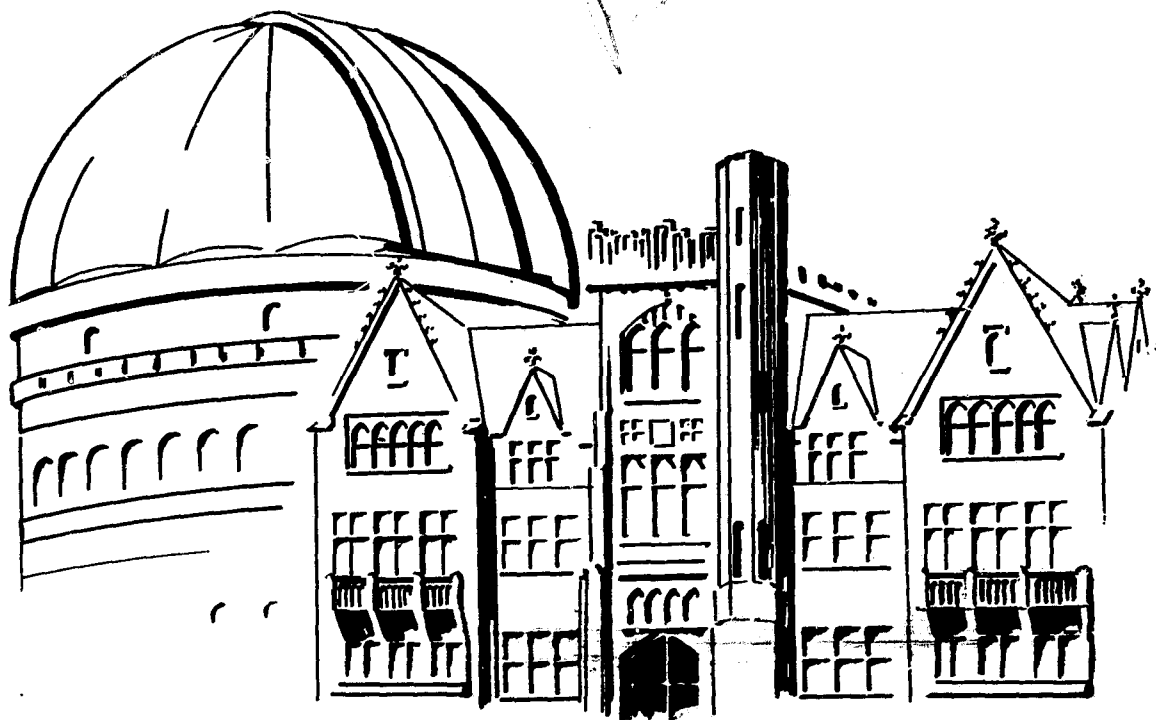


## General Disclaimer

### One or more of the Following Statements may affect this Document

- This document has been reproduced from the best copy furnished by the organizational source. It is being released in the interest of making available as much information as possible.
- This document may contain data, which exceeds the sheet parameters. It was furnished in this condition by the organizational source and is the best copy available.
- This document may contain tone-on-tone or color graphs, charts and/or pictures, which have been reproduced in black and white.
- This document is paginated as submitted by the original source.
- Portions of this document are not fully legible due to the historical nature of some of the material. However, it is the best reproduction available from the original submission.



Department of  
**ASTRONOMY and ASTROPHYSICS**  
**UNIVERSITY of CHICAGO**

Preprint No. 165

MASS LOSS IN RED GIANTS  
AND SUPERGIANTS

by

Fred Sanner

Oct 14 1975

(NASA-CR-145435) MASS LOSS IN RED GIANTS  
AND SUPERGIANTS (Yerkes Observatory) 98 p  
HC \$4.75 CSCI 03A

**RYERSON PHYSICAL LABORATORY**

1100 East 58th Street  
Chicago, Illinois 60637

**YERKES OBSERVATORY**

N76-10940 Williams Bay  
Wisconsin 53191

Unclas  
G3/83 42933

**MASS LOSS IN RED GIANTS AND SUPERGIANTS**

**Fred Sanner\*  
Yerkes Observatory  
University of Chicago**

**\*Present address: Kitt Peak National Observatory,  
Tucson, Arizona.**

## ABSTRACT

The circumstellar envelopes surrounding 13 late-type giants and supergiants have been studied using a homogeneous collection of high resolution, photoelectric scans of strong optical resonance lines. A method for extracting the circumstellar from the stellar components of the lines allows a quantitative determination of the physical conditions in the envelopes and of the rates of mass loss at various positions in the red giant region of the HR diagram.

The strengthening of the circumstellar spectrum with increasing luminosity and later spectral type is probably caused by an increase in the mass of the envelopes and not by decreased ionization of the metals. The mass loss rate for individual stars is proportional to the visual luminosity. The high rates for the supergiants suggest that mass loss is of fundamental importance to the evolution of these stars. The bulk of the mass return to the interstellar medium in the red giant region comes from the normal giants, with a rate comparable to that of the planetary nebulae. There is evidence in the line profiles that the envelopes are spatially and kinematically complex.

## I. INTRODUCTION

Mass loss from stars is of interest with regard to both stellar evolution and the evolution of the Galaxy as a whole. Schwarzschild (1961) has stressed the importance of knowing quantitative rates of mass loss in accurate calculations of the advanced stages of stellar evolution (Rood 1973). Also, whether massive stars ultimately evolve into white dwarfs or into supernovae depends on their ability to shed mass in excess of the Chandrasekhar limit prior to exhaustion of nuclear energy sources. Schmidt (1959) and Quirk and Tinsley (1973) have shown that the exchange of mass between stars and the interstellar medium governs the statistical properties of the different stellar populations, as well as the density and chemical composition of the interstellar medium.

Adams and MacCormack (1935) first noted asymmetries in some of the strong optical resonance lines of the M stars  $\alpha$  Ori,  $\alpha^1$  Her,  $\alpha$  Sco and  $\beta$  Peg. At a dispersion of  $5.6 \text{ \AA mm}^{-1}$ , they found that the cores of the photospheric lines were systematically displaced to the blue by about  $5 \text{ km s}^{-1}$ . They suggested that the line shifts were caused by the absorption of photospheric light in a gradually expanding gaseous envelope around the star. In a study of the  $\alpha$  Her binary system, Deutsch (1956) observed sharp absorption lines in the spectrum of the G0III companion at the heliocentric velocities of the strongest circumstellar (CS) lines of the primary. He concluded that the companion lay within the envelope of the M

**PRECEDING PAGE BLANK NOT FILMED**

star. At the estimated separation of the companion, matter is capable of escaping from the system. He inferred that mass is being lost from all M stars having displaced resonance line cores. No entirely satisfactory mechanism for driving the mass loss has yet been identified (Weymann 1963, Wickramasinghe et. al. 1966, Fix and Alexander 1974).

Deutsch (1960) later surveyed the red giant region of the HR diagram and found the presence of a CS shell to be a property common to these stars. He suggested that the principal return of mass to the interstellar medium may occur in this region. Using blue coude spectrograms at a dispersion of  $4.5 \text{ \AA mm}^{-1}$ , he outlined the qualitative behavior of the CS line systems with spectral type and luminosity class. At M0III the only CS lines are those of Ca II H and K (see also Wilson 1960). These lines strengthen with progressively later spectral type and increasing luminosity until the Ca I  $\lambda 4227$  and the Sr II  $\lambda 4078$  and  $\lambda 4216$  resonance lines appear. In the most highly developed systems, resonance lines of the low abundance metals K I, Na I, Al I, Ti I, Cr I, Mn I, Fe I, Sc II, Ti II, and Ba II are present, as well as several low excitation lines of Al I, Ti I, Fe I, Sc II, and Ti II, indicating a very low state of excitation in the envelopes. He also found a correlation between the CS H and K line velocity displacement and spectral type for normal giants. In studies of the supergiants  $\rho$  Cas and  $\alpha$  Ori, respectively, Sargent (1961) and Weymann (1962) determined quantitative mass loss rates and physical conditions in the CS envelopes from  $1.9 \text{ \AA mm}^{-1}$  photo-

graphic data, using analyses based on the curve of growth for pure scattering in a plane atmosphere. Using data covering 25 years, Weymann found that the absorption components in Betelgeuse neither varied measurably in strength nor shared the radial velocity variations of the underlying photospheric lines, indicating that the shell is detached from the photosphere.  $\rho$  Cas, on the other hand, apparently ejected its CS envelope in 1957 (Bidelman and McKellar 1957) and has undergone several sporadic mass loss episodes since.

Over the past decade, observations of infrared emission at  $11 \mu$  (Woolf and Ney 1969) and of  $H_2O$  and OH maser emission in the radiofrequency spectrum (Schwartz and Barrett 1970; Wilson et. al. 1970) have indicated the presence of dust and molecular components in the CS envelopes surrounding the latest and most luminous stars. Very recently, Goldberg et. al. (1975) have observed the CS spectrum of  $\alpha$  Ori at high resolution ( $2 \text{ km s}^{-1}$ ) and have reported fine structure in the absorption components of K I  $\lambda 7699$  and of the Na I D lines.

The present study is a reexamination of the mass loss phenomenon in late type giants and supergiants, based on a homogeneous collection of high resolution, photoelectric scans of various optical resonance lines in 13 stars. The purpose of the program is to determine the quantitative behavior of the CS features, and from them to infer (1) the density, temperature, extent, degree of ionization, and kinematics of the envelopes, (2) the rates of mass loss, and (3) the relations between these quantities and the properties of the central stars. Such relations

may provide insight into the mass loss mechanism and serve as constraints on theories of the acceleration process.

## II. OBSERVATIONS

### a) The Program

The program is restricted to selected naked-eye stars having well developed CS spectra, and includes 8 bright M, K and G supergiants, all with highly developed CS systems, and 5 nearby M giants with weaker CS lines (Table 1). Each of these stars has an asymmetry in at least one program line of each type discussed below, allowing the full solution for the shell properties. A number of additional M giants and K and M supergiants having circumstellar H and K lines did not display such a complete array of asymmetric photospheric cores. These stars are presumably surrounded by less massive envelopes, or were observed at a time when the photospheric line velocity made detection of CS components difficult. Also, several other K and M giants were searched unsuccessfully for evidence of mass loss. Stars having one or more symmetric program lines are listed in Table 2.

Basic data for the program stars is summarized in Table 1. Spectral types and notes on heavy metal abundances have kindly been provided by Dr. P. C. Keenan (private communication; Morgan and Keenan 1973). Absolute visual magnitudes, bolometric corrections, and effective temperatures are determined from the spectral types using the calibration of Lee (1970). The quantities



$E(B-V)$  and  $A_{HK}$ , the interstellar extinction in magnitudes at the Ca II H and K lines, are derived from observed and intrinsic colors (Johnson et. al. 1966; Lee 1970) and the standard interstellar extinction curve. Distances for  $\alpha$  Sco,  $\mu$  Cep, 6 Gem and VV Cep are determined assuming association membership; for the other stars they are derived from the distance moduli and reddening corrections. Radii are derived from the measured angular diameters where available (Gezari et. al. 1972) and from the bolometric corrections and effective temperatures otherwise.

In addition to the presence of CS absorption lines, the stars in Table 1 have several other properties in common. All are variable in broad band magnitudes (Kukarkin 1969) and several are known radial velocity variables. Chromospheric emission in the H and K lines of Ca II (Wilson and Bappu 1957) and in the Fe II lines between  $\lambda\lambda 3150$  and  $3300$  arising from multiplets 1, 6, and 7 (Herzberg 1948, Bidelman and Pyper 1963) has been detected in most of the program stars.  $\mu$  Cep, 6 Gem and  $\alpha$  Ori show marked infrared excesses at  $11 \mu$  (column 12) and may have significant dust components in their envelopes (Gehrz and Woolf 1971), while  $\alpha$  Sco and  $\alpha^1$  Her have slight infrared excesses. The envelopes of the other stars are almost entirely gaseous. For stars where measurements are available, the variation in the degree of polarization of visible light  $\langle |\Delta P| \rangle$  is correlated with the intensity of the Ca II K-line chromospheric emission, listed in column 15 (Dyck and Johnson 1969; Jennings and Dyck 1972). The mean degree of polarization  $\langle P \rangle$  is correlated with the infrared

excess (Dyck et. al. 1971).  $\alpha$  Sco, VV Cep, and  $\alpha^1$  Her are binaries with early-type companions. Table 3 summarizes the pertinent data. The mass of the primary in the VV Cep system has been derived from a calculation of the orbit (Cowley 1969 and references); accurate masses for all other program stars remain undetermined.

The strengths of the various lines in a CS system are sensitive to different physical conditions in the corresponding envelope. Three distinct types of CS lines therefore have been observed for each star. First, at least one line in a dominant ionization state is observed (the "metal" line). The total column density inferred for this species can then be scaled, assuming cosmic abundances, to give the total column densities in the envelope for all elements. The H and K lines of Ca II fall into this category. However, they are strongly saturated in the stars studied here. The profiles are further complicated by the presence of chromospheric emission and absorption, as well as possible interstellar contamination. Their analysis for the calcium column densities is therefore highly uncertain. These lines also lie far enough to the blue to make count rates at the needed resolution extremely low for cool stars. In contrast, the corresponding resonance lines of Sr II at  $\lambda 4078$  and  $\lambda 4216$ , and of Ba II at  $\lambda 4554$  and  $\lambda 4934$ , are unsaturated in these stars and have no known interstellar or chromospheric contributions. The line strengths vary approximately in the ratios 1:2:4:8 from red to blue, so that measurements of both doublet pairs allow good estimates of shell column densities over two orders

of magnitude. One or more of these four lines has been measured for each program star.

The assumption of cosmic abundances for Ba and Sr is questionable in red giants, since s-process neutron capture in the interiors of some red giants is capable of increasing the abundances of Ba, Sr, Zr, and other elements with magic neutron numbers relative to the abundances of the lighter elements (Burbidge and Burbidge 1957). Ba II and S stars show enhancements in the lines observed here. In M stars, blending around Ba II  $\lambda 4554$  and Sr II  $\lambda 4078$  is so severe that any photospheric overabundance must be large before it can be noticed. ZrO band strength is also an indicator of heavy metal enhancement. Unfortunately, ZrO is so sensitive to temperature and Ba II to luminosity that it is difficult to single out the abundance effects in relative changes in line strength from star to star. Dr. Keenan has inspected coude spectrograms of the program stars and found that none are pronounced Ba II or S stars;  $\alpha$  Ori,  $\rho$  Per,  $\beta$  Peg and  $\alpha$  Sco, however, may have mild Ba-Sr enhancement. From a curve of growth study, Boesgaard (1970) derived a mean heavy-metal overabundance by a factor of 6 for typical Ba II stars. Thus, an overabundance by a factor of perhaps 2 or 3 is possible in these 4 stars. If this effect is present, the mass loss rates of these stars will be overestimated by a similar factor, through overestimates of both the hydrogen column densities and the sizes of the shells. Electron densities will be underestimated.

The Ca II infrared triplet lines at  $\lambda\lambda 8498, 8542, \text{ and } 8662$  comprise a second type of line observed (the "triplet" lines). They arise from an excited, metastable lower level which is

radiatively populated. Because Ca II is a dominant ionization state, the strengths of these lines relative to the metal lines are sensitive primarily to the distance of the shell from the central star.

Finally, a third type of CS line which has been observed is one arising from a trace ionization state (the "trace" lines). The ratios of the strengths of these lines to the metal lines can be used to infer the degree of ionization in the shells. Na and K are among the elements most easily ionized in the shells, in view of the steep decrease of the stellar radiation into the ultraviolet. The Na I D lines  $\lambda 5890$  and  $\lambda 5896$ , and the corresponding K I lines  $\lambda 7665$  and  $\lambda 7699$ , were chosen for this reason, and because of their accessibility and line strengths, which vary approximately in the ratios 1:2:22:44 from red to blue. The much less saturated K I lines are generally more useful. Strong interstellar components may contaminate the profiles of the Na I lines in the more distant stars; the corresponding components at the K I lines are much weaker (Hobbs, 1974).  $\lambda 7665$  was observed in only one star ( $\mu$  Cep) owing to severe  $O_2$  telluric interference there; near both D lines (especially  $\lambda 5890$ ) important atmospheric  $H_2O$  lines are also present.

#### b) The Scans

The scans are shown in Figure 1. They were obtained from 1972 to 1975 using the double-pass echelle scanner at the coude focus of the 107-inch (2.7-m) telescope at the McDonald Observa-

tory. The observations were accumulated until 3000 or more counts were reached in the line cores. Typical scans extend over  $3 \text{ \AA}$ , with 2 data points per resolution element. The resolution (FWHM) of the triplet, metal, and Na I line scans is generally  $4 \text{ km s}^{-1}$ , although several supplemental scans at resolutions of  $2 \text{ km s}^{-1}$  and better were obtained for the brightest stars. The K I line cores were measured at a resolution of  $2 \text{ km s}^{-1}$ . Photospheric and telluric line identifications (Table 4) are from Davis (1946) and Moore et. al. (1966). Interstellar lines are identified with less certainty and are listed in Table 8. Because the CS features lie in the cores of strong resonance lines, corrections for scattered light and dark count can be critical in determining the strength of the CS absorption, especially in the blue. A filter containing  $\text{CuSO}_4$  solution was used in scanning the metal lines, and an RG-8 filter was used in obtaining the triplet scans. Day-sky scans of the cores of H and K and of the atmospheric A band at  $\lambda 7603$  with these filters verify that contamination from scattered light and from other orders is negligible. A correction for the light of the binary companions was applied to the scans of  $\alpha \text{ Sco}$  and VV Cep using relative energy distributions for the spectral types of Table 3 (Straizys et. al. 1972) scaled by the visual magnitudes.

Additional lower resolution scans of the triplet lines extending over  $30 \text{ \AA}$  were obtained to establish the continuum level. The scans in Figure 1 are normalized to this level, on a scale of residual intensity. The Na I and K I lines are normalized to an estimated local continuum, on an approximate scale of residual intensity. In the regions of the metal lines, the

continuum is not well defined owing to line blanketing. These scans are presented on arbitrary scales of relative intensity.

Figure 1 shows the general presence of the systematically blue-shifted CS components in the program lines. The variety in appearance of the cores results from differences in the relative widths and line center displacements of the CS and photospheric components, the strength of the CS feature, and the resolution. The strongest CS features, especially in the cores of relatively narrow photospheric lines (Sr II  $\lambda 4216$ , the trace lines, and all of the lines of  $\rho$  Cas), consistently take on the form of P Cygni profiles superimposed on the cores of the resonance lines. The presence of emission shifted redward of line center strongly suggests that the gas is indeed CS, extending at least several stellar radii above the photosphere.

Figure 2 shows a superposition of the Sr II  $\lambda 4078$  and  $\lambda 4216$  scans of the giant stars. The strengthening of the CS asymmetry with spectral type and luminosity can be seen in both lines, in spite of severe blending in  $\lambda 4078$ . The Na I D lines are stronger than Sr II  $\lambda 4078$  in the giants and very much stronger in the supergiants. The weaker Ca II triplet lines are generally comparable in strength to the Ba II lines.

At resolutions of  $2 \text{ km s}^{-1}$  and higher, some of the absorption components in the trace and triplet lines are resolved into detailed structure, indicating that the CS cores are formed in a region which is spatially and kinematically complex on a small scale. In addition, scans of various lines obtained on different nights indicate that these features vary in at least 5 of the stars.

At present there is not sufficient data to study how these variations are correlated from line to line and with the variability of the central stars, or to assess the importance of these small scale features to the mass loss phenomenon as a whole.

The unresolved photographic data show that the general asymmetric nature of the lines has persisted for decades, indicating that the outflowing envelope is in a steady state on a large scale, to some extent. In the present study, the  $4 \text{ km s}^{-1}$  data will be used to analyse the mass loss phenomenon in terms of a homogeneous, steady state envelope, which may approximate the large scale behavior of the shells in a statistical way. The effects of this assumption on some of the quantitative conclusions will be discussed in the appropriate sections.

### III. THE MODEL ENVELOPE

In order to infer column densities and kinematic information about the envelopes, it is necessary to separate the CS from the stellar components in the scans of Figure 1. Since the shell is detached from the photosphere of the central star, it is meaningful to consider the stellar radiation incident on the inner surface of the shell as a background "continuum". The separation is carried out by determining the proper choice of this unknown continuum. The choice will be guided in part by considerations of the transfer of line radiation through a detached, extended model envelope (§ IV a and b). The CS profiles obtained in this way are analysed for column densities and kinematic information (§ IV c). Physical properties are then derived from the various

column densities and their ratios (§ V).

Although both the shell geometry and kinematics are unknown in advance, some restrictions can be placed on the models considered. If the shells are in the form of disks, a distribution of inclination angles might be expected, and some of the envelopes would be seen face-on. In these cases, the CS profile would consist of symmetric emission at line center. Profiles of this type have not been reported for late-type stars. Further, the spatial distribution of the program stars relative to the sun is highly concentrated to the galactic plane, with  $|b| < 20^\circ$  for 11 of them. If these shells were in the form of disks, the systematic presence of blue-shifted asymmetries would force alignment of the disks roughly parallel to the galactic plane.

In view of the systematic blue shift observed for all stars and of the fewer parameters needed, it will be assumed that the shells are spherically symmetric.

Observations of the  $\alpha$  Her system indicate that the material has a roughly constant outflow velocity to the escape distance. Deutsch (1960) and Weymann (1962) found no strong evidence for velocity gradients in the shells, with the possible exceptions of the displacements in the Na I D and Ca II H and K lines. H and K are systematically shifted to the blue in giants and to the red in supergiants, relative to the other CS lines. Reimers (1975) has suggested the presence of a velocity gradient in the shells of normal giants on the basis of this behavior. He explains the high velocity of H and K relative to the other lines as owing to



their formation further out in the shell where the matter has been accelerated to a terminal velocity plateau. The present observations can be interpreted without this assumption, and a more careful treatment of the extremely saturated H and K profiles seems to be needed for their interpretation (§ V a). It will be assumed that the gas has a Maxwellian distribution of "turbulent" velocities and an expansion velocity which are independent of position in the shell. The ratio of the expansion velocity to the root mean square turbulent velocity is defined as

$$\gamma \equiv \frac{V_e}{V_t} \quad (1)$$

In a uniform, steady state flow having spherical symmetry and constant expansion velocity, the density, as determined by the conservation of matter, varies with distance from the central star as  $r^{-2}$ . The physical detachment of the shell from the photosphere is accounted for by assuming that the CS material lies above some radius  $d_0 \geq R^*$ , where  $R^*$  is the photospheric radius. The intervening region may be filled with matter in a different physical condition (e.g. a chromosphere). The parameter  $d_0$  is assumed the same for all atomic species. The total density in the shell at distance  $r$  from the central star is therefore

$$n(r) = n(d_0) \left(\frac{d_0}{r}\right)^2, \quad r \geq d_0. \quad (2)$$

This model gives the simple relations

$$N_i = n_i(d_0) d_0 \quad (3)$$

and

$$\dot{M} = 4\pi m_H N_H V_e d_0 (1 + \eta) , \quad (4)$$

where  $N_i$  is the total column density of atom  $i$ ,  $\dot{M}$  is the rate of mass loss, and  $\eta$  accounts for the mass of the elements heavier than hydrogen. A typical Population I value for  $\eta$  of 0.42 is adopted here. Two related parameters which will be useful in the radiative transfer calculations are the dilution factor  $W$  and the optical depth  $\tau_0^{ij}$  at the center of a line arising from level  $i$  with upper level  $j$ . They are given by

$$W(r) = \frac{1}{2} \left[ 1 - \left( 1 - \frac{R_*^2}{r^2} \right)^{1/2} \right] \quad (5)$$

and

$$\tau_0^{ij} = \frac{N_i}{V_t} \left( \frac{\sqrt{\pi} e^2}{m_e c} \right) f^{ij} \lambda^{ij} , \quad (6)$$

where  $N_i$  is the column density of atoms in the lower level and  $\lambda^{ij}$  is the wavelength of the transition. Equation (6) follows from the fundamental relation between the oscillator strength  $f^{ij}$  and the absorption coefficient  $\alpha_\nu$ ,  $\int_0^\infty \alpha_\nu d\nu = \frac{\pi e^2}{m_e c} f^{ij}$ .

Both  $N_i$  and  $d_0$  will be obtained from the observations, so that equations (3) and (4) then provide the central results of the present analysis.

#### IV. ANALYSIS OF THE LINE PROFILES

##### a) The Important Atomic Levels and Processes

Such an expanding, extended envelope affects the radiation of the central star by interconverting photons among the various lines

and continua of a given atom, and by redistributing photons over a frequency range of about  $2\gamma$  Doppler units within the individual lines. When  $\gamma$  is on the order of unity, line reemission by the shell readily fills in the absorption, and the composite profiles are complex and saturate at small optical depths. In such cases, a meaningful equivalent width cannot be defined and a curve of growth is not applicable. In the present analysis, column densities and kinematics are obtained instead by fitting theoretical line profiles to the high resolution data. The trace and triplet lines are sufficiently resolved for this procedure, since the instrumental resolution element is much less than  $2\gamma$ . In contrast, the CS profiles of the metal lines are only marginally resolved. Supplementary high resolution scans of some of these lines do not reveal significant instrumental broadening in the lower resolution data, or the presence of additional fine structure in the line profiles. Profile fitting therefore can be safely applied to this data also.

The emergent CS line profiles depend on the envelope parameters and the distribution of sources through the shell. In a model with this particular velocity law, computed profiles can also depend upon the assumptions made concerning the redistribution function. Magnan (1968) has studied the effect in the case of a uniform distribution of sources for a model with  $d_0 \gg R^*$  and  $\gamma = 1$ . At  $\tau_0 = 20$ , the differences between the profiles computed with exact and with complete redistribution are small compared to the accuracy with which profiles can be determined from the present data. Further, the optical depths of the lines in the present study

are generally much lower, on the order of unity. For a different model, Robbins (1968) found that the difference in the mean number of scatterings between angle-averaged exact redistribution and complete redistribution diminished with decreasing optical depth. If this effect holds generally, then the present assumptions of complete redistribution and isotropy of the source function should be an excellent approximation in the profile-fitting procedure.

The depth dependence of the line source function is determined by the energy level structure of the ion and by the frequency dependence of the incident stellar radiation. After analyses of various model atoms, the important processes and levels have been isolated. Because of similarities in their atomic structure, Ca II, Sr II, and Ba II are considered together; a similar but separate treatment holds for Na I and K I. Table 5 summarizes the pertinent data for the observed atoms.

For all the program stars, optical depths at the centers of the Ba II and Sr II resonance lines are on the order of unity or less. The line transfer is dominated by single scattering of direct stellar photons between the  $^2S$  and  $^2P$  levels, followed by escape from the shell. Radiative transition rates from the  $^2S$  and  $^2P$  levels to higher levels and the continuum are negligible because of the low radiation intensity shortward of  $3000\text{\AA}$  in M stars. The low degree of ionization in the envelope ( $\xi V c$ ) makes recombination to all levels negligible. Collision rates with electrons and neutral hydrogen atoms (Mihalas 1973; Bahcall and Wolf 1968) have been included and are also negligible. The

population of the  $^2D$  metastable levels can become important, however, even if the shells are optically very thin in the resonance lines. In this case, the relative populations of the metastable levels are essentially independent of the dilution factor. Given the incident stellar radiation in the lines, the fraction of ionized Ba and Sr in these levels is calculated to be on the order of 0.2 and 0.04 respectively. A scan of the  $\lambda 6142$  line of Ba II in  $\alpha$  Ori shows no CS component, consistent with this estimate of the populations and the observed CS line strength of Ba II  $\lambda 4554$ .

Optical depths in the K line of Ca II, determined by scaling those of the Ba II and Sr II resonance lines, lie in the range 400 ( $\beta$  Peg) to 60,000 ( $\rho$  Cas). Optical depths in the triplet lines are generally on the order of unity or less, while the shell is optically very thin in the forbidden lines. A five level atom in which radiative rates dominate provides an accurate description of the populating mechanism of the Ca II levels. At the excitation temperatures indicated by the observed ratio of metastable to ground populations, and at the maximum densities inferred by setting  $d_0 = R^*$  in equation (3), collision rates with hydrogen atoms and with electrons are negligible, except between the fine structure levels.

Details of this calculation which affect the determination of the dilution factor are deferred to § V a. With regard to the formation of the triplet line profiles, it will be noted here that 1) the scattering in these lines conserves photons to a high degree, and 2) when the shell is optically thin in these lines, the profiles depend upon only the column densities and kinematics of the model envelope.

For Na I and K I, the ionization balance has been solved simultaneously with the resonance line transfer by adding a continuum. Optical depths at the centers of the strongest K I  $\lambda 7699$  lines may exceed 10. The recombination and photoionization rates to and from the  $^2S$  and  $^2P$  levels are very small relative to the scattering rates, and the transfer of line radiation decouples from the ionization balance over a wide range of electron density. Recombination emission is negligible in this model. However, various fluorescent mechanisms may be operating in these atoms. Bidelman and Pyper (1963) have noted that the Fe II emission lines at  $\lambda 3303$  in  $\rho$  Per and other M stars are weakened relative to the other Fe II lines by CS Na I resonance line absorption at  $\lambda \lambda 3302$  and  $3303$ . Also, strong chromospheric emission in the Mg II lines at  $\lambda \lambda 2796$  and  $2803$  lines is responsible for about one third of the total photoionization rate from the ground level (Doherty 1972a). Observations of the K I  $\lambda 7699$  lines in  $\alpha$  Ori, 119 Tau,  $\alpha^1$  Her and possibly  $\psi^1$  Aur show variability of the emission components of the CS profiles, indicating a variable population of the  $^2P_{1/2, 3/2}$  levels in the envelopes. The statistical equilibrium model adopted here is oversimplified in these cases.

#### b) The Stellar Continuum

The CS components of the scans are separated from the stellar components by making two assumptions. One is related to the transfer of radiation in the envelope; the other, to the transfer in the photosphere. First, from the considerations of § IV a, pure scattering is an excellent approximation to the line transfer in the

shells. This approximation holds over a wide range of shell temperature, hydrogen density, electron density and kinematics, for all the program lines except K I  $\lambda 7699$ . In short, the CS lines are formed by redistribution of the photospheric line cores into P-Cygni features. If the star does not occult a significant portion of the receding half of the shell and if the shell is unresolved by the telescope slit, then a distant observer must find the number of photons in net emission relative to the stellar continuum equal to the number in net absorption. Second, it is assumed that the underlying photospheric line is symmetric. This also appears to be an excellent approximation, with the possible exception of  $\mu$  Cep. These two assumptions govern the interpolation of the stellar continuum across the line cores, and allow the CS profiles to be obtained directly from the data, independently of uncertainties about the proper models for the photosphere and the envelope.

In practice, the separation is unambiguous in the cases of the Na I D lines, Ba II  $\lambda 4934$  and Sr II  $\lambda 4216$  since the CS feature acts as a small perturbation on an unblended photospheric line. Chromospheric emission in the Ca II H and K lines suggest that triplet lines in a number of K and M giants and supergiants with strong H and K emission and weak or absent shell lines have symmetric cores (Table 2). It will be assumed that any chromospheric contribution in the stars with shell spectra is also symmetric about line center. Blending of Fe I  $\lambda 4554.460$  with Ba II  $\lambda 4554$  may affect the separation of this profile in a few stars. Blends mask all but the core of Sr II  $\lambda 4078$ . However, they permit accurate determination

of the line center, and the separation has been performed differentially among the program stars. The stellar K I  $\lambda 7699$  line is badly masked by the CS component in the supergiants, making separation of this profile ambiguous. The column density of neutral potassium is therefore determined with less certainty than those of the other ions. K I  $\lambda 7665$  and  $\lambda 7669$  deserve careful future study in this regard because of the information they convey on kinematics, variability, ionization balance and condensations in the envelopes (see § V c).

The adopted stellar continua in several lines are shown in Figure 3. In addition to defining the CS profiles, these continua give the relative frequency dependence of the stellar radiation incident on the shell. If absolute spectrophotometry is available to establish the actual intensities, then the distribution of sources of line photons within the shell can be written

$$S(r) = 2 \int_{-\infty}^{\infty} N_{\nu}(R^*) W(r) \left\{ \exp[-\tau_0(r) \exp(-v^2)] \right\} \kappa_0(r) \exp(-v^2) dv. \quad (7)$$

Here  $S(r)$  is the rate per unit volume at which photons are deposited at point  $r$  and  $N_{\nu}(R^*)$  is the photon flux normalized to the stellar surface at a frequency  $\nu$  Doppler units from line center, measured in the reference frame at  $r$  moving with the gas.

The quantity  $\kappa_0(r)$ , the local linear absorption coefficient at line center, is related to the line center optical depth by

$\tau_0(r) = \int_{d_0}^r \kappa_0(x) dx.$  In the triplet and metal lines,  $N_{\nu}(R^*)$  varies by at most a factor of 2 across the CS profiles, and the underlying continuum in equation (7) is assumed to be constant. In the case of K I  $\lambda 7699$ , the frequency variation of  $N_{\nu}(R^*)$  may



have important effects on the calculated profiles. The stellar continuum is not well determined for these lines, however, so it has been assumed constant in this case also.

### c) The Column Densities and Kinematics

The radiative transfer and statistical equilibrium equations have been solved simultaneously for each ion by means of an integral equation (Capriotti 1964). The resulting theoretical emission and absorption profiles seen by a distant observer have been calculated for each program line. Details are given in the Appendix.

For optically thin CS lines (e.g. the triplet and metal lines) the shapes of the theoretical profiles depend only on the envelope parameters  $\tau_0$  and  $\gamma$ . The model profiles are compared with the profiles obtained from the scans to determine the acceptable range of these parameters for each line. When optical depths exceed unity, the line profiles are also affected by the distribution  $S(r)$ . The shell parameters inferred in these cases (i.e. from some of the K I and Na I resonance lines) may not be well determined, owing to the schematic nature of the model envelope.

A representative set of profiles, computed for various  $\tau_0$  at a fixed value of  $\gamma$ , is shown in Figure 4. As  $\tau_0$  increases, the velocity of minimum residual intensity moves blueward; this velocity always exceeds the expansion velocity. When the absorption component of the profile saturates, the composite profile develops a secondary bump near line center. If this effect is responsible for the step at the center of the K I lines in the supergiants

$\psi^1$  Aur and 119 Tau, then line center optical depths may exceed 10. The effects of varying  $\gamma$  are shown in Figure 5, which gives the relations between the minimum residual intensity and  $\tau_0$  for several values of  $\gamma$ . In the limiting case  $\gamma \gg 1$ , there is no reemission into the line of sight within the line core (the interstellar case). This limit is useful in setting rigorous lower limits on the column densities.

In general, the profile of a massive, slowly expanding envelope can mimic that of a thinner shell having a larger expansion velocity. This effect is illustrated in Figure 6, which shows two profiles which have been fit to the Ba II  $\lambda 4554$  line of 6 Gem. In stars where two lines arising from the same lower level have been observed, the range of acceptable pairs  $(\tau_0, \gamma)$  can be restricted by the additional constraints  $\tau_0(1) = \frac{1}{2} \tau_0(2)$  and  $\gamma(1) = \gamma(2)$ . Once a profile is fit,  $V_e$  and  $V_t$  follow from  $\gamma$  and the scale of the observed profile. The velocity  $V_e$  measures expansion about the center of mass, and is not the differential expansion of the shell relative to the photosphere at the time of observation. Column densities follow from  $\tau_0$  and  $V_t$  using equation (6). The column densities and kinematics for various acceptable choices of  $\gamma$  are listed in Table 6. The symmetric lines listed in Table 2 are useful in supplementing these results by providing lower limits on the column densities of certain levels.

Characteristic values of  $\gamma$  in the envelopes lie in the range  $\frac{1}{2}$  to 2. The corresponding column densities vary by a factor of about 6. The intermediate value  $\gamma = 1.35$  will be adopted for illustrative

purposes in the figures below. The inferred physical conditions are not so sensitive to the particular choice of  $\gamma$ . Both  $d_0$  and  $n_e$  are determined by the ratios of column densities in different lines (§ V a and c). If it is assumed that  $\gamma$  has roughly the same value for all the lines in a given envelope, then these ratios do not depend upon the assumed kinematics. The mass loss rate is proportional to the product  $N_H V_e$  obtained from one of the metal lines (§ V b). This product varies by a corresponding factor of about 3.

Figures 7 and 8 show the correlations of  $N_H$  and  $V_e$ , respectively, with  $M_V$  of the central star. In Figure 7,  $N_H$  has been determined by scaling the column densities of the metals by the normal abundance ratios. This relation extends, in quantitative terms, Deutsch's observation that CS line strength increases with stellar luminosity. In Figure 8, expansion velocities have been grouped according to line type. For the metal and trace lines, there is no marked change of the expansion velocity with luminosity. The triplet line velocities, however, increase with luminosity, from values typical of the metal lines in the normal giants to velocities greater by a factor of 1.5 in the supergiants. An alternative interpretation is that the expansion velocities in all the lines are comparable, but that the triplet lines have larger turbulent velocities in the supergiants. This effect will be discussed further in § V a.

It is interesting to note that the expansion velocity determined for  $\rho$  Cas is intermediate between those of the K and M supergiants of Table 1 and those of the F supergiants 89 Her and FU Ori (Deutsch

1968). Also, the column densities of Sr and Ba in the envelope of  $\alpha$  Her are in the ratio 4.2:1, in accord with their relative cosmic abundance.

## V. PHYSICAL PROPERTIES OF THE ENVELOPES

### a) The Distances of the Shells

Weymann (1962) first suggested that the infrared triplet lines  $\lambda\lambda 8498, 8542$  and  $8662$  of Ca II might be useful in determining the distance of the CS material from the star. He argued that the metastable Ca II levels are populated in the shell by stellar radiation in the lines, appropriately diluted according to shell distance; the strengths of the CS lines arising from the ground level (e.g. the other program lines) instead are independent of the absolute fluxes in the shell, and do not vary with the dilution factor. He was unable to detect an asymmetry in the  $\lambda 8542$  line of  $\alpha$  Ori and concluded that the shell must be separated from the star by at least 14 stellar radii.

At sufficiently high resolution, all the program stars show asymmetries in one or more of the triplet lines (Figure 1). In the giants, the asymmetry weakens progressively along the sequence  $\lambda\lambda 8542, 8662, 8498$ ;  $\lambda 8498$  is often symmetric. In the supergiants, the asymmetries in  $\lambda 8542$  and  $\lambda 8662$  are comparable in strength, while that in  $\lambda 8498$  is weaker.

At a resolution of  $4 \text{ km s}^{-1}$  the line profiles are variable. Scans of  $\lambda 8542$  in Betelgeuse obtained over a period of 3 years show net blueward absorption of up to  $70 \text{ m}\text{\AA}$ . Net red shifted absorption

is present in several scans. These variations occur over a time scale of months or less and may be due in part to the observed radial velocity shifts of about  $10 \text{ km s}^{-1}$  of the underlying photospheric line. Similar behavior is observed in the stars  $\rho$  Per, R Lyr and  $\beta$  Peg. Except for  $\rho$  Cas, these lines do not show marked CS emission, in contrast to the profiles of the metal and trace lines.

At resolutions of  $2 \text{ km s}^{-1}$  and better, the triplet line profiles in several of the stars (Figures 1 and 9) show fine structure components. Scans of  $\lambda 8542$  and  $\lambda 8662$  in Betelgeuse obtained on the same night (Figure 9) show weak features at heliocentric velocities of  $+19$  and  $+30 \text{ km s}^{-1}$ , with strengths of  $9$  and  $8 \text{ m}\text{\AA}$  in  $\lambda 8542$  and  $<4$  and  $6 \text{ m}\text{\AA}$  in  $\lambda 8662$ . The strengths and velocities of these components are variable.

#### i) Excitation of the Metastable Levels

The column density in the metastable level may be written

$$\frac{N_m}{N_1} = \int_0^{\tau_0} \frac{n_m}{n_1}(\tau) \frac{d\tau}{\tau_0}, \quad (8)$$

where  $\frac{n_m}{n_1}(\tau)$  gives the variable excitation as a function of depth in the shell. This ratio depends on several quantities: the optical depth  $\tau_0(K)$  at the center of the K line, the expansion velocity parameter  $\gamma$ , and, ultimately, the stellar radiation incident on the shell. The first two quantities have been determined (Table 6) by the profile fitting analysis described above. The third depends both upon the inner shell radius  $x_0 = d_0/R^*$  (i.e. the dilution factor), and upon the absolute intensities in the 7 Ca II

lines at the stellar photosphere. These intensities, which are required in equation (7), have been measured for each program star, as described below. Thus the ratio  $\frac{N_m}{N_i}$  can be used to determine  $d_0$ .

The absolute intensities in the 7 Ca II lines were measured with the big scanner at the Cassegrain focus of the 82-inch (2.1-m) Struve reflector at the McDonald Observatory on the nights of October 27 and 28, 1973. In the red, photometry was obtained of the continua near the triplet and forbidden lines at a resolution of  $17 \text{ \AA}$ . Intensities in the cores of the triplet lines were determined by scaling these measurements with the core residual intensities of the extended triplet scans. Photometry of the H and K line cores was obtained at a resolution of  $6 \text{ \AA}$ . These intensities were converted to absolute fluxes at the stellar photosphere using the data of Table 1.

Since the envelope is optically thin in the triplet and forbidden lines, the radiation fields in the envelope are simply the direct stellar radiation fields diluted by the factor  $W$  in equation (5). Radiation in the H and K lines includes both direct and diffuse components. In general, the optical depths in the H and K lines are sufficiently small to allow H and K photons to diffuse through the shell and escape. The populations of the  $^2D$  and  $^2P$  levels depend on the details of this diffusion, which effectively couples the local population ratios with those in other parts of the shell. As noted above, the populations were obtained by means of an integral equation assuming complete redistribution and an isotropic source function.

The transfer of radiation in the lines and the excitation of the metastable levels can be illustrated with reference to Figure 10. This figure shows a plot of the predicted Ca II column densities in the  $^2D$  levels as a function of the inner shell radius  $x_0$ , for R Lyr, as determined from equation (8). At large distances from the star, the curves approach values calculated assuming detailed balance in the H and K lines, with  $N(^2D_{5/2})/N(^2S_{1/2}) \propto x_0^{-2}$ . In this limit the metastable levels are populated directly by absorption and emission of forbidden line photons, and indirectly by absorption of stellar H and K photons, which scatter on the order of 10 times before decaying to the metastable level. Depopulation occurs by forbidden line emission. Radiation in the  $\lambda 8498$  line is so dilute that the two line groups H- $\lambda 8662$ - $\lambda 7323$  and K- $\lambda 8542$ - $\lambda 7291$  are transferred independently in two decoupled three-level atoms. The relative populations of the  $^2D_{3/2}$  and  $^2D_{5/2}$  levels are in the ratio of the sources for these cycles. As  $x_0$  decreases, the stellar intensity in the triplet lines increases and ions are more readily returned to  $^2P$  from the metastable level. Effective scattering in H and K increases, until eventual migration to a "boundary" permits escape. The H and K radiation fields in the shell, and consequently the populations of the  $^2D$  levels, are thus smaller than in the case of detailed balance. For a given value of  $x_0$ , this effect is more pronounced in the H radiation field since the shell is optically thinner in this line. When H photons scatter  $\gtrsim 100$  times,  $\lambda 8498$  radiation couples the two three-level cycles, resulting in conversion of H to K. For  $x_0 \lesssim 3$ , the cycles are completely mixed

and the populations are roughly in the ratio of the number of scatterings in K to H, or about 2. This conversion results in substantial emission in K at the expense of net absorption in H. The net emission in the triplet lines is about  $10^{-3}$  times smaller than the intensity in the photospheric line core.

For a given star, the computed ratio  $\frac{N_m}{N_1}$  is essentially independent of the variables  $\tau_0(K)$  and  $\gamma$  within the range inferred from the corresponding CS line profiles. In contrast,  $\frac{N_m}{N_1}$  is roughly proportional to the total incident stellar intensity in the resonance and forbidden lines. The CS triplet line strengths will therefore vary with the central star, for a fixed value of the inner shell radius  $d_0$ . There is not sufficient data at hand, however, to verify this predicted correlation. In this regard, it should be noted that the H and K photometry of the supergiants has been corrected for interstellar extinction by a factor of up to 10 in scaling the fluxes to the stellar surface. Uncertainties in this correction lead to corresponding uncertainties in the inferred values of  $d_0$ .

The sensitivity of the solution to the assumption of complete redistribution can be estimated in the following way. For fixed incident stellar radiation fields in the lines, the column densities in the metastable levels increase with the mean number of scatterings in H and K. Magnan (1968) and others have shown that the mean number of scatterings with exact redistribution is greater than the number with complete redistribution. Complete redistribution therefore provides an underestimate of  $N_m/N_1$ . On the other hand, the



maximum possible number of scatterings in H and K occurs in the case of detailed balance, independent of assumptions concerning the redistribution function, since photons are thermalized in the shell before they escape. This case provides an overestimate to  $N_m/N_1$ . Both cases have been calculated and are shown in Figure 10. For a given column density ratio, the error in the inferred  $d_0$  owing to this assumption is always less than a factor of 2.

ii) Results

The calculated column density ratio  $\frac{N_m}{N_1}$  must be compared with the observed ratio, in which the column density  $N_m$  is obtained from the CS triplet profiles and  $N_1$  is estimated by scaling the column densities of Ba II and Sr II by the normal abundance ratios. Table 7 lists the resulting inner shell radii and the corresponding densities, given by equation (3). The shells of the giants are separated from the central stars by from 2 to 4 stellar radii. The boundaries of the supergiant shells are separated by slightly larger values, typically 5 stellar radii. In absolute units,  $d_0$  increases with the visual luminosity  $L_v$  in such a way that

$$\left( \frac{d_0}{2.2 \times 10^{13} \text{ cm}} \right)^2 = \frac{L_v}{L_v(M_v=0)} \quad (9)$$

Apparently, the shells adjust their size so that the incident visual flux at the inner boundary has a constant value  $8 \times 10^{-36}$  ergs  $\text{cm}^{-2} \text{ s}^{-1} \text{ \AA}^{-1}$ . At a typical separation of  $3 \times 10^{14}$  cm from a supergiant of  $20 M_\odot$ , the escape velocity is  $30 \text{ km s}^{-1}$ . The CS envelopes are therefore likely to be gravitationally bound to the central stars, unless additional forces are acting on them to cause mass loss.

In addition to inferring  $d_0$  from the column densities in the individual triplet lines, it may be independently inferred (with less accuracy) from the relative populations of the  ${}^2D_{5/2}$  and  ${}^2D_{3/2}$  levels, when observations of both  $\lambda 8542$  and  $\lambda 8662$  are available. With reference to Figure 10, the giant stars, with stronger asymmetries in  $\lambda 8542$ , yield shell separations less than about 5 stellar radii. In the supergiants, the comparable strengths of the two lines imply separations between 5 and 15 stellar radii.

Within the envelopes the populations of the  ${}^2D$  levels vary approximately as  $r^{-4}$ , as compared with  $r^{-2}$  for the ground level. The CS cores of the triplet lines are therefore formed closer to the star than are the optically thin metal lines. Half the contribution to the core strength arises below  $x = 1.2 x_0$  and  $2.0 x_0$ , respectively. The triplet lines may therefore be useful in probing the inner regions of the shell near the chromosphere. If the fine structure in the profiles is related to mass ejection from the chromosphere into the shell, further study of these lines may lead to a better understanding of the details of the acceleration process. Also, because they are formed nearer the star, the triplet line profiles may be affected to a larger extent than the metal lines by the occultation of the receding half of the shell by the star, particularly in the giants. This may account in part for the absence of marked emission in these lines. No simple picture emerges for the H and K line profiles, since conversion of H into K operates at these dilution factors.

The tendency for the expansion velocity inferred from the triplet lines to exceed those of the metal lines in the supergiants (§IV c) may

indicate that the shell material decelerates as it moves outward through the region  $d_0 \lesssim r \lesssim 2 d_0$ . From Figure 8, the velocity shift in this region is on the order of the expansion velocity.

This implies a deceleration of

$$\frac{dv}{dt} = \frac{dv}{dr} \frac{dr}{dt} \sim \frac{V_e^2}{d_0} \sim 10^{-2} \text{ cm s}^{-2},$$

If, on the other hand, there is a gradient in the turbulent velocity, an outward acceleration of about the same magnitude would result from the gradient in kinetic energy density. At a separation of  $3 \times 10^{14}$  cm from a supergiant of  $20 M_\odot$ , this acceleration is comparable to the acceleration needed to balance the gravitational attraction of the central star. Hence, the envelope may convert the energy in local random motions into the systematic radial flow. It is especially interesting to note in this regard that the width of the chromospheric K line emission feature increases in a well defined way with stellar visual luminosity, and has a typical value of about  $150 \text{ km s}^{-1}$  in red supergiants (Wilson and Bappu 1957).

#### b) Rates of Mass Loss

The rates of mass loss are determined from equation (4) using  $N_H$  and  $V_e$  inferred from the metal lines and  $d_0$  from the triplet lines. The product  $N_H V_e$  is accurate to a factor of about 3, judging from values based on different lines of the same doublet. The inner shell radius is probably accurate to a factor of 2. Therefore, within the framework of the present treatment, the inferred mass loss rates should lie typically within a factor of 5 of the value listed in Table 7 for  $\gamma = 1.35$ . The actual mass loss rate may differ from this estimate by a larger factor, depending on the abundance of

the metals relative to hydrogen and on the effects of departures from the schematic model envelopes.

The mass loss rate varies with the luminosity and spectral type of the central star. Figure 11 shows the relationship between mass loss rate and  $M_V$ . The corresponding relation between mass loss rate and visual luminosity (excluding the stars  $\alpha$  Sco and VV Cep) is

$$\dot{M} (M_{\odot} \text{ yr}^{-1}) = 3.6 \times 10^{-9} \frac{L_v}{L_v(M_v=0)} \quad (10)$$

For normal giants of the same absolute magnitude ( $\beta$  Peg and  $\rho$  Per;  $\delta^2$  Lyr and  $\alpha^1$  Her), the mass loss rate increases by a factor of roughly 2.5 for each spectral subtype from M2 to M5. This dependence on spectral type not well determined, owing to the small range in spectral type represented by the stars in Table 1. The corresponding relations for mass loss in the physical HR diagram are

$$\log \dot{M} (M_{\odot} \text{ yr}^{-1}) = -9.9 (\pm 0.3) - 0.51 (\pm 0.05) M_{bol},$$

based on all the stars but  $\alpha$  Sco and VV Cep, and

$$\dot{M} (M_{\odot} \text{ yr}^{-1}) \propto T_{\text{eff}}^{-8},$$

based on the two giants  $\beta$  Peg and R Lyr.

The mass loss rate is also well correlated with the intensity of the chromospheric emission in the K line, as shown in Figure 12. This correlation may not be insured by the correlation between  $\dot{M}$  and  $M_V$  since, in general,  $I_K$  is not uniquely determined by  $M_V$  (Wilson and Bappu 1957). Weaker correlations exist between the gaseous component of the shells, as indicated by  $N_H$  and  $\dot{M}$ , and the dust component, as measured by the infrared excess at  $11 \mu$  and the

change in polarization of visual light. However, these do not appear to be independent (§II a). Hence, the mass loss rate is determined by at least two and possibly three parameters related to the central star and its chromosphere. In the following, it will be assumed that the program stars are typical of their spectral types and luminosities, and that  $\dot{M}$  is fixed by these two properties. The relations above may prove useful in determining the importance of mass loss to both stellar and galactic evolution. Also implicit in them is an understanding of the underlying forces responsible for the mass loss.

Detailed calculations of stellar evolution explicitly incorporating these relations are not yet available. For the present, an estimate can be made by comparing the dynamical evolution rate discussed by Schwarzschild (1961) and given by equation (10) with the nuclear evolution rate, given by the rate of hydrogen consumption (in grams per second) assuming that the total stellar luminosity arises from hydrogen burning. In general the mass loss rate is comparable to the nuclear consumption rate for the luminous giants. The relative importance of mass loss increases with increasing luminosity; the mass loss rate of  $\rho$  Cas exceeds the hydrogen consumption rate by a factor of about 6. It appears that mass loss is of fundamental importance to the evolution of the most luminous stars. A similar conclusion follows if it is assumed that the mass loss rate given by equation (10) persists over a timescale for evolution in the red giant region of about  $10^7$  years.

The total rate of mass return to the interstellar medium in a

column perpendicular to the galactic plane is given by

$$\dot{m} = \int N(M_V) \dot{M} dM_V ,$$

where  $N(M_V)$  is the number of stars  $\text{pc}^{-2}$  in a unit interval of  $M_V$ .

From equation (10), the luminosity function in the solar neighborhood (Allen 1973), and scale heights of 400 parsecs and 78 parsecs for the giants and supergiants, respectively (Blanco 1965; Lee 1970), the local rate of mass return from normal M giants and G, K, and M supergiants is  $\dot{m} = 4.4 \times 10^{-11} M_{\odot} \text{pc}^{-2} \text{yr}^{-1}$ .

This rate does not include the contribution from the Mira variables.

If it is assumed that these stars follow the relation between  $\dot{M}$  and spectral type found above, then the mass loss rate for a typical Mira of class M7 with  $M_V=0$  (Allen 1973) is approximately 10 times greater than that for R Lyr, or about  $1 \times 10^{-7} M_{\odot} \text{yr}^{-1}$ . For the space density and scale height adopted by Gehrz and Woolf (1971), the estimated rate of return for these stars is  $3 \times 10^{-11} M_{\odot} \text{pc}^{-2} \text{yr}^{-1}$ , comparable to that of the normal giants. However, the extrapolation of  $\dot{M}$  to spectral subtypes this late should be considered with caution. Osterbrock gives  $1.5 \times 10^{-10} M_{\odot} \text{pc}^{-2} \text{yr}^{-1}$  as the rate of mass return from planetary nebulae within a radius of 1000 parsecs of the sun, and a rate for supernovae approximately two orders of magnitude less. In view of the uncertainties in these estimates, it appears that the mass loss rate from stars in the red giant phase of evolution is comparable to the rate from stars in the planetary nebulae stage.

Equations (9) and (10) suggest that the cool, slow CS flows in the envelopes of the red giants are regulated by the stellar visual luminosity. Together, they imply that the mass flux has a constant

value of approximately  $6 \times 10^{-37} \text{ gm cm}^{-2} \text{ s}^{-1}$ . It will be interesting to extend high resolution observations of the optical lines over a wider range of stellar types, including the Mira variables, to investigate the generality of the relations between  $\dot{M}$  and the properties of the central star found above, and to study the dependence of mass loss rate on stellar variability.

### c) Ionization in the Shells

The behavior of the CS line spectrum in the sequence of envelopes across the red giant region depends on the change in ionization with spectral type and luminosity. It is important to determine whether the weakening of the CS spectrum with increasing effective temperature is a reflection of increasing ionization of the metals or decreasing shell mass. It will be assumed that photoionization is the principal means of ionization.

From the Ba and Sr line strengths, typical column densities for the shells are  $\sim 10^{21} \text{ cm}^{-2}$  for hydrogen and  $10^{16} \text{ cm}^{-2}$  for the metals. For photoionization cross sections of  $10^{-18} \text{ cm}^2$ , the shell is optically thick in the Lyman continuum and optically thin in the metal continua. Hydrogen ionization at the inferred densities could be maintained only if the intensity of radiation in the Lyman continuum were to exceed that at the peak of the stellar energy distribution near  $1 \mu$ . The emission measure of such a region would be  $\int n_e n_p dr \sim 10^{10} \text{ cm}^{-6} \text{ pc}$ , capable of producing Balmer emission lines detectable against the stellar photosphere. These lines have been observed in VV Cep

(Cowley 1969) and  $\mu$  Cep (McLaughlin 1946). In the former case, photoionization by the nearby companion is probably responsible; in the latter, the emission is weak and present only at maximum light. It probably arises in the chromosphere through collisional excitation rather than photoionization. Hence, with the exception of VV Cep, the shells considered here must be H I regions in which metals are the principal electron donors.

The degree of ionization of the metals depends on the relative importance of the direct stellar and the interstellar radiation fields in the ultraviolet. The only observations of ionizing flux for these stars available at present are broadband magnitudes in the range 1910 Å to 3120 Å for  $\alpha$  Ori and  $\beta$  Peg (Doherty 1972b). In the cases of Na and K, with photoionization edges at  $\lambda\lambda$ 2410 and 2860, respectively, stellar radiation dominates. The stellar ionizing rate for the other abundant metals is unknown; if the interstellar field dominates, the high densities will prevent their ionization.

The ratios of neutral to total column densities for Na and K indicate that these atoms are almost completely ionized. Assuming that ionization equilibrium holds (but see Weymann 1962), the electron density at position  $r$  in the shell can therefore be written

$$n_e = \frac{n^0}{n} \frac{\Gamma(R^*)W(r)}{\alpha(T)}, \quad (11)$$

where  $n_e$ ,  $n^0$  and  $n$  are the local electron, neutral atomic and total atomic densities,  $\Gamma(R^*)$  is the photoionization rate at the stellar surface, and  $\alpha(T)$  is the recombination coefficient to all levels



(Seaton 1951). If the degree of ionization is assumed to be constant with radius, the ratio of local densities in equation (11) may be replaced by the ratio of column densities inferred from Table 6. The electron density is then determined by the product  $\Gamma(R^*)W(d_0)$ . The photoionization rates have been calculated for  $\alpha$  Ori and  $\beta$  Peg from

$$\Gamma(R^*) = \int_0^{\lambda_p} N_\lambda(R^*) \sigma_\lambda d\lambda,$$

where  $\lambda_p$  is the wavelength of the photoionization edge. The measured photoionization cross sections  $\sigma_\lambda$  of Hudson (1964) and Hudson and Carter (1965) were used, and the stellar photon flux  $N_\lambda(R^*)$  has been approximated by a series of trial spectra which reproduce the OAO-2 colors. For  $\alpha$  Ori and  $\beta$  Peg,  $\Gamma_{Na}(R^*) = 1.5 \times 10^{-8} \text{ s}^{-1}$  and  $3.2 \times 10^{-8} \text{ s}^{-1}$  respectively. The K I photoionization rates are greater by a factor of 2. Ionization rates for the remaining stars have been estimated by scaling those of  $\alpha$  Ori by the ratio of visual fluxes at the stellar surfaces, taking no account of changes in color. Contributions to  $\Gamma$  in the vicinities of the stars with binary companions have been calculated using energy distributions for the appropriate spectral types (Evans 1972 and Underhill 1972) and the data of Table 3. Values of  $\Gamma$  and the degree of ionization calculated for a temperature of  $10^3$  °K are listed in Table 7. In view of the uncertainties in the column densities of the trace lines, and in the estimates of the photoionization rates for the single stars, the degree of ionization is only roughly determined.

The degree of ionization in the shells of the single stars is lower than that in the interstellar medium, owing to the much higher densities. Na, Ca and Al, and in some stars Fe and Mg, are the

principal electron contributors. In the  $\alpha$  Her system, the companions are sufficiently cool and distant to have negligible effect on the ionization balance. The companion of  $\alpha$  Sco is at roughly the same separation, but is early enough in type to ionize C, N and O (and hence Ba<sup>+</sup>, Sr<sup>+</sup>, and Ca<sup>+</sup>) near the primary. In VV Cep, the companion is probably capable of ionizing hydrogen down to the surface of the M star. Second ionization of the metals in these two envelopes makes estimates of the hydrogen column density, and hence the mass loss rate, lower limits. On the other hand, if Ca and Ba are ionized to the same extent, then the calculation of  $d_0$  based on the triplet lines is unaffected.

C, N, and O are neutral in the shells surrounding the single stars. If the gas is heated by photoionization of the metals and cooled by fine structure emission from these elements, then the resulting equilibrium temperature is less than 100°K. A similar temperature is indicated in the outer parts of the envelope of  $\alpha$  Her by the relative strengths of the CS features at  $\lambda\lambda 3944$  and  $3962$  of Al I, and by the absence of CS cores in lines arising from the excited fine structure levels of Fe I (Burgess, Field and Michie 1960).

By making certain simplifying assumptions, the trace and metal line column densities can be used to place an upper limit on the dilution factor. Using equation (3), equation (11) can be written in the form

$$\frac{N_e}{N_H} = \frac{1}{2} \frac{N_K^0}{A_K N_H^2} \frac{\Gamma(R^*) R^*}{\alpha(T) X_0},$$

where  $A_K$  is the cosmic abundance of K relative to hydrogen. For a star of given trace and metal line strengths, the degree of

ionization decreases with increasing shell size. Since Na I is a trace ionization state in  $\alpha$  Ori and  $\beta$  Peg, a lower limit to the degree of ionization follows if Na is assumed to be the principal electron donor. The corresponding upper limits for  $d_0$  in these stars are  $12R^*$  and  $5.6R^*$ , respectively. This result is unique to the assumption of constant ionization and to the density distribution of equation (2), in which the scale height equals  $d_0$ . More generally,  $n_e/n_H$  varies as  $\frac{\Delta}{d_0^2}$ , where  $\Delta$  is the shell thickness, so that  $d_0$  can exceed these estimates only if the scale height increases at least as fast as  $d_0^2$ .

At resolutions better than  $2 \text{ km s}^{-1}$ , additional sharp absorption components are resolved in the K I and Na I lines. They appear either as fine structure in the absorption cores of the P Cygni profiles or as sharp isolated lines blueward of it. It is unlikely that interstellar and telluric absorption accounts for all of them. These features are listed in Table 8. The K I scans of  $\mu$  Cep are particularly striking in this regard (Figure 9), with 4 additional components displaced  $40 \text{ km s}^{-1}$  to the blue of the photospheric line. Corresponding features have been observed by Deutsch in the stronger resonance lines of Fe I and in Ca I  $\lambda 4227$  (Weymann 1963), but are absent in the  $\lambda 4554$  and  $\lambda 8542$  scans in Figure 1. The appearance of these features primarily in the lines of the neutral metals indicates the presence of high density condensations in the envelopes, analogous to those in planetary nebulae and in the interstellar medium, in which recombination drives most of the metals into the neutral state. Lines of the various atoms therefore

are formed in regions of differing density, depending on the abundance of the atom and its degree of ionization ( $\Gamma[R^*]W$ ). If K I is a dominant stage of ionization in the  $40 \text{ km s}^{-1}$  condensations, this knot contains 1% of the total number of atoms in the line of sight. More likely, K I is partially ionized, making this estimate a lower limit. High resolution profiles of the Fe I, Ca I, Al I, K I and Na I lines obtained over a period of several years may be useful in separating the interstellar from CS components and in studying the distribution of densities and sizes of the condensations. If a significant fraction of the Ba and Sr atoms are found to lie within these condensations, the inferred hydrogen column densities and rates of mass loss will have to be increased correspondingly.

#### d) The Effects of CS Dust

The presence of dust in the CS envelopes of some stars (e.g.  $\delta$  Gem,  $\mu$  Cep and  $\alpha$  Ori) may have an appreciable effect on their optical CS line spectra. Since the optical properties of grain material are poorly known, and it is not known to what extent the gas and dust coexist, a quantitative analysis is not attempted here. Measurable effects are expected when the thermalization optical depth in the lines owing to grain opacity exceeds unity. It will be assumed that the grain opacity is continuous and increases to the blue.

Grain opacity can affect both the line profiles and the populations of radiatively excited levels. In the analysis of the line profiles of § IV c, the normalized absorption profile will not be strongly affected by grains, since the neighboring continuum under-

goes the same extinction. Emission, however, is extinguished as grain opacity increases, since the shell traps photons in a region in which they can be absorbed. This effect will be more pronounced in the optically thicker lines. In the limit in which all photons are absorbed, there is no shell reemission (the interstellar case). The presence of marked emission in the metal and trace lines of the giants, and in the lines of  $\rho$  Cas, is consistent with the absence of excess infrared emission in these stars. The presence of strong infrared excesses in the shells of 89 Her and the Be stars (Gillett et. al. 1970; Sargent and Osmer 1969) is also consistent with the general presence of emission lines only in the red and near infrared spectral regions. Emission in the  $\lambda 4554$  lines of  $\mu$  Cep and  $\alpha$  Ori seems to indicate that the optical depth of dust at this wavelength cannot be very much greater than unity. Further to the blue, dust may appreciably alter the diffusion of H and K radiation if it absorbs photons before they escape from the envelope. With increasing dust opacity, the triplet lines weaken relative to the resonance lines. The large value of  $x_0$  inferred for  $\mu$  Cep may be partly due to this effect.

## VI. SUMMARY

The present work is a study of the envelopes surrounding 13 late type giants and supergiants. Various macroscopic properties of the envelopes, including the mass loss rate, dilution factor, hydrogen density, and degree of ionization, have been determined quantitatively. The results have been derived under the funda-

mental assumptions of

- 1) spherical geometry,
- 2) steady state,
- 3) the presence of the metals in their cosmic abundances, and
- 4) symmetry of the underlying photospheric lines.

The results are the following.

- 1) The rate of mass loss is directly proportional to the visual luminosity of the central star for red giants and supergiants. It increases by a factor of roughly  $2\frac{1}{2}$  for each spectral subtype from M2 to M5 for normal giants.
- 2) The mass loss rate increases with decreasing intensity of the chromospheric emission in the K line.
- 3) The bulk of the CS material lies within a few radii of the central star. The shells increase in size with visual luminosity (for the M stars) in such a way that the visual stellar flux incident on them is a constant.
- 4) The degree of ionization in the envelopes of single stars does not vary significantly within the red giant region, with  $n_e/n_H \sim 10^{-6}$ . Na, Al and Ca, and in some stars Fe and Mg, are the principal electron donors. The presence of early-type binary companions alters the ionization balance in varying degree, depending on the spectral type of the companion and its separation from the primary.
- 5) The rate of mass loss is comparable to the rate of hydrogen consumption in the supergiants, if hydrogen burning is responsible for most of the stellar luminosity. Mass loss

is likely to be fundamentally important to the evolution of the most luminous stars.

- 6) The total rate of mass return to the interstellar medium in the solar neighborhood by M giants earlier than M5 and by G, K, and M supergiants, is  $4.4 \times 10^{-11} M_{\odot} \text{ yr}^{-1}$ .
- 7) There may be an acceleration on the order of  $10^{-2} \text{ cm s}^{-2}$  in the supergiants owing to a decrease in the turbulent velocity with distance from the star.
- 8) At high resolution, the CS profiles are resolved into multiple velocity components which vary on a time scale of months. The envelopes are composed in part of cold, high density condensations.
  - a) K I and other trace neutrals may be useful in conjunction with the metal lines in determining the spectrum of density fluctuations and their kinematics.
  - b) The Ca II triplet lines may be a useful probe of the chromosphere-shell transition region. Further studies of the profiles of these lines may lead to an understanding of the mass acceleration process.

I am grateful to Dr. Leo Goldberg for providing results in advance of publication, Dr. W. W. Morgan for several stimulating discussions, Dr. P. C. Keenan for providing insight into the problem of the heavy metal abundances, and the staff of McDonald Observatory for their assistance at the telescope. I especially express my

sincere thanks to Dr. L. M. Hobbs for encouragement and advice throughout the course of this work.

This work was supported in part by grant NGR 14-001-147 from the National Aeronautics and Space Administration.



## APPENDIX

### a) Definition of the Problem

The transfer of radiation in the CaII resonance and subordinate lines through an expanding, extended CS envelope is especially interesting, since 1) although H and K are the dominant optical CS lines, the behavior of their profiles with luminosity and spectral type is not understood, and 2) the strengths of the CS line cores in the triplet depend on the diffusion of H and K radiation in the shell. A detailed calculation was performed in an effort to understand the formation of these lines.

The population of the metastable levels is governed by the H and K thermalization rate, or equivalently by the emission of forbidden radiation. The probability of thermalization at each scattering depends principally on the intensity of triplet radiation in the shells. These probabilities are on the order of  $5 \times 10^{-5}$  near the stars and increase to a maximum of 0.09 at large distances. For shells with  $\tau_0 < 10^4$  the thermalization rate is determined by scattering in the Doppler core, since the wings are optically thin. For larger  $\tau_0$ , the populations of the metastable levels are determined to a greater extent by the transfer of line radiation in the wings as  $x_0$  increases from unity. The detailed calculation of these effects, incorporating both wing and core opacity and including the partial coherence of scattering in the wings, is beyond the scope of this study. However, since the optical depths are not excessively large, these effects should not be large. The problem has therefore been solved in detail for scat-

tering within the Doppler core only. The additional population of the metastable levels arising from thermalization in the damping wings will be estimated separately.

b) The Transfer Equation

The diffuse radiation field at a point  $\vec{r}$  is calculated in a coordinate system moving with the gas. With reference to the geometry of Figure (A1),  $r \equiv |\vec{r}|$ ,  $r' \equiv |\vec{r}'|$ ,  $R \equiv \frac{r}{d_0}$ ,  $R' \equiv \frac{r'}{d_0}$ ,

$$\sin \phi = \frac{R}{R'} \sin \theta \quad \text{and} \quad S^2 = R^2 + (R')^2 + 2RR' \cos(\theta - \phi).$$

The equations will be written in terms of the optical depth at line center measured radially outward from  $d_0$ ,

$$\tau_{0,ij}(r) = \int_{d_0}^r \kappa(x) dx = \tau_{0,ij} \left(1 - \frac{d_0}{r}\right) \delta^{ij}, \quad \text{where (see Equation 6)} \quad \delta^{ij} = \left(\frac{\sqrt{\pi} e^2}{m_e c} \frac{f^{ij} \lambda^{ij}}{V_t}\right)^{-1}.$$

For constant outward expansion, the radial velocity in Doppler units between points  $\vec{r}$  and  $\vec{r}'$  is  $V_{rad}(\vec{r}, \vec{r}') = \gamma(\cos \phi - \cos \theta)$ .

Thus, the gas in the volume element at  $\vec{r}'$  emits a redshifted profile  $\frac{\epsilon_v(R') \exp\{-[\nu + \gamma(\cos \phi - \cos \theta)]^2\}}{\sqrt{\pi}} \equiv \epsilon_v(R') \frac{\exp(-\nu'^2)}{\sqrt{\pi}}$  photons  $\text{cm}^{-3} \text{s}^{-1} \Delta\nu^{-1}$  as seen at  $\vec{r}$ . Intervening gas elements P along the direction of radiation present distributions of absorbers  $\exp\{-[\nu + \gamma(\cos \theta - \cos \phi)]^2\}$ , which attenuate the beam. The optical depth along the path, written in terms of the angle variable  $t$ , is thus

$$\tau(R, R', \theta, \nu; \gamma, \tau_0) = \frac{\tau_0}{R \sin \theta} \int_{\phi}^{\theta} \exp\{-[\nu + \gamma(\cos t - \cos \theta)]^2\} dt.$$

At  $\vec{r}$ , the linear opacity coefficient,  $\exp(-\nu^2) \frac{\tau_0 d_0}{r^2} \text{cm}^{-1}$ , therefore gives rise to a volume absorption rate of diffuse radiation

$$A_v^d(R) = \epsilon_v(R') \int_{-\infty}^{\infty} \frac{\exp(-\nu'^2)}{\sqrt{\pi}} \frac{\exp[-\tau(R, R', \theta, \nu)]}{4\pi S^2} \exp(-\nu^2) \frac{\tau_0 d_0}{r^2} d\nu$$

due to emission in the volume element at  $\vec{r}'$ . The absorption rate at  $\vec{r}$  resulting from emission from a shell of unit thickness at

fixed  $\vec{r}'$  is found by integrating over  $\theta$  and azimuth:

$$A_v^d(R) = \frac{1}{d_0} \mathcal{E}_v(R') \left(\frac{R'}{R}\right)^2 K(R, R'), \quad (A1)$$

where

$$K(R, R'; \tau_0, r) = \tau_0 \int_0^\pi \int_{-\infty}^\infty \frac{\exp(-\nu')^2}{\sqrt{\pi}} \frac{\exp[-\tau(R, R', \theta, \nu)]}{2 S^2} \exp(-\nu)^2 d\nu \sin\theta d\theta.$$

In this form, the kernel is independent of the radius  $d_0$ . It will be convenient to consider the corresponding relation between absorption and emission rates in shells of unit optical thickness.

By defining the shell rates  $A_s^d(\tau) = A_v^d(R) \times (\text{shell volume})$

$$= A_v^d(R) 4\pi r^2 \frac{dr}{d\tau} = A_v^d(R) 4\pi r^2 \frac{r^2}{\tau_0 d_0},$$

the equation of transfer becomes

$$A_s^d(\tau) = R^2(\tau) \int_0^{\tau_0} \mathcal{E}_s(\tau') K(\tau, \tau') d\tau'. \quad (A2)$$

### c) The Emission Coefficient

The volume emission coefficient at  $\vec{r}'$  is related to the population density of the upper level  $n^j(\vec{r}')$  through  $\mathcal{E}_v(\vec{r}') = n^j(\vec{r}') E^{j\lambda}$ , where  $E^{j\lambda}$  is the Einstein coefficient for spontaneous emission.

In terms of the rates per unit shell, and using equation (2) for the ground state population,

$$\mathcal{E}_s(\tau') = \frac{n^j}{n^i}(\tau') E^{j\lambda} \frac{g^{i\lambda}}{W(\tau')}.$$

The local excitation equilibrium for the atom can be written

$$\frac{n^j}{n^i} = \sum_{k=2}^5 A_a^{ik} \alpha_{kj}, \quad (A3)$$

where  $A_a^{ik}$  is the total (direct stellar plus diffuse) absorption rate per atom in lines connecting levels  $k$  with the ground state,  $\alpha_{kj}$  ( $k \neq j$ ) is related to the probability that absorption of a  $1k$  photon ultimately leads to population of level  $j$  without

first having returned to the ground state, and  $\alpha_{HK}$  is related to the probability of direct scattering. The  $\alpha_{Rj}$  are functions of the atomic constants and the radiation in the triplet lines. In the present problem, the shells are optically thin to triplet radiation, and hence  $A(\tau) = A^* W(\tau)$ . The  $\alpha_{Rj}$  are therefore known functions of  $d_0$  and  $\tau'$ . For the K line (levels are identified in

Table 5)

$$\Sigma_s^K(\tau) = (A_a^{12} \alpha_{25} + A_a^{13} \alpha_{35} + A_a^H \alpha_{45} + A_a^K \alpha_{55}) E^{51} \frac{\delta^{15}}{W}$$

The first 2 terms represent absorption of direct stellar forbidden radiation, as given in equation (7). The total rates for H and K can be separated into their direct and diffuse contributions  $A_a^H = A_a^{H,*} + A_a^{H,d}$ . Grouping the terms in this way,

$$\Sigma_s^K = S_s^{K,*} + A_s^{H,d} B^{HK} \frac{\delta^K}{\delta^H} + A_s^{H,d} B^K, \quad (A4)$$

where

$$S_s^{K,*} = (A_a^{12} \alpha_{25} + A_a^{13} \alpha_{35} + A_a^{H,*} \alpha_{45} + A_a^{K,*} \alpha_{55}) E^{51} \frac{\delta^{15}}{W}, \quad (A5)$$

$$B^{HK} = \alpha_{45} E^{51}$$

is the H to K conversion probability, and  $\frac{\delta^K}{\delta^H} = \frac{f^H}{f^K} \frac{\lambda^H}{\lambda^K} \approx \frac{1}{2}$ ,

Redefining the shell emission rate (A4)  $\Sigma_K = S_K + \frac{1}{2} A_H B_{HK} + A_K B_K$ ,

equation (A2) takes the form

$$A_K(\tau) = R^2(\tau) \int \Sigma_K(\tau') K(\tau, \tau') d\tau',$$

In terms of  $\Sigma(\tau)$ , the corresponding coupled integral equations for the H and K radiation fields are

$$\begin{aligned} \varepsilon_H(\tau) - 2 \varepsilon_K(\tau) \frac{B_{KH}(\tau)}{B_K(\tau)} &= \sigma(\tau) B_H(\tau) R^2(\tau) \int \varepsilon_H(\tau') K_H(\tau, \tau') d\tau' \\ &+ S_H(\tau) - 2 S_K(\tau) \frac{B_{KH}(\tau)}{B_K(\tau)} \end{aligned} \quad (A6)$$

and

$$\begin{aligned} \varepsilon_K(\tau) - \frac{1}{2} \varepsilon_H(\tau) \frac{B_{HK}(\tau)}{B_H(\tau)} &= \sigma(\tau) B_K(\tau) R^2(\tau) \int \varepsilon_K(\tau') K_K(\tau, \tau') d\tau' \\ &+ S_K(\tau) - \frac{1}{2} S_H(\tau) \frac{B_{HK}(\tau)}{B_H(\tau)}, \end{aligned}$$

where

$$\sigma(\tau) = \left( 1 - \frac{B_{HK}(\tau) B_{KH}(\tau)}{B_H(\tau) B_K(\tau)} \right).$$

d) The Method of Solution

Equations (A5) have been solved numerically by replacing the integrals over optical depth with 6 and 10 point Gaussian quadrature formulae over the variable  $\alpha = \frac{2\tau}{\tau_0} - 1$ , with the corresponding weights  $W_\alpha$ . The equation for the H line is thus

$$\epsilon_H(\tau_i) - 2 \epsilon_K(\tau_i) \frac{B_{KH}(\tau_i)}{B_K(\tau_i)} = \sigma(\tau_i) B_H(\tau_i) R^2(\tau_i) \sum_{j=1}^N \epsilon_K(\tau_j) K_H(\tau_i, \tau_j) \frac{1}{2} W_\alpha(\tau_j) + S_H(\tau_i) - 2 S_K(\tau_i) \frac{B_{KH}(\tau_i)}{B_K(\tau_i)}$$

In the terms in which  $j=i$  an integration across the singularity in the kernel at  $\tau=\tau_i$

is required. The singularity is removed by subtracting the equation

$$\sigma(\tau_i) B_H(\tau_i) R^2(\tau_i) \epsilon_H(\tau_i) \int K(\tau_i, \tau') d\tau' = \sigma(\tau_i) B_H(\tau_i) R^2(\tau_i) \epsilon_H(\tau_i) \sum_{j=1}^N K(\tau_i, \tau_j) \frac{1}{2} W_\alpha(\tau_j)$$

and setting terms of the form

$$\sigma(\tau_i) B_H(\tau_i) R^2(\tau_i) [\epsilon_H(\tau_i) - \epsilon_H(\tau_i)] K_H(\tau_i, \tau_i)$$

equal to zero. Grouping coefficients,

$$\begin{aligned} \epsilon_H(\tau_i) \left\{ 1 - \sigma(\tau_i) B_H(\tau_i) R^2(\tau_i) \left[ \int K_H(\tau_i, \tau) d\tau - \sum_{i \neq j} K_H(\tau_i, \tau_j) \frac{1}{2} W_\alpha(\tau_j) \right] \right\} - 2 \epsilon_K(\tau_i) \frac{B_{KH}(\tau_i)}{B_K(\tau_i)} \\ = \sigma(\tau_i) B_H(\tau_i) R^2(\tau_i) \sum_{i \neq j} \epsilon_H(\tau_j) K_H(\tau_i, \tau_j) \frac{1}{2} W_\alpha(\tau_j) + S_H(\tau_i) - 2 S_K(\tau_i) \frac{B_{KH}(\tau_i)}{B_K(\tau_i)}. \end{aligned} \quad (A7)$$

In matrix notation, (A7) can be written

$$\begin{aligned} \begin{bmatrix} M_H \\ \end{bmatrix} \begin{bmatrix} \epsilon_H \\ \end{bmatrix} + \begin{bmatrix} M_{HK} \\ \end{bmatrix} \begin{bmatrix} \epsilon_K \\ \end{bmatrix} &= \begin{bmatrix} S_H \\ \end{bmatrix} \\ \begin{bmatrix} M_K \\ \end{bmatrix} \begin{bmatrix} \epsilon_K \\ \end{bmatrix} + \begin{bmatrix} M_{KH} \\ \end{bmatrix} \begin{bmatrix} \epsilon_H \\ \end{bmatrix} &= \begin{bmatrix} S_K \\ \end{bmatrix}, \end{aligned} \quad (A8)$$

and

where

$$M_{H}^{ij} = -\sigma(\tau_i) B_H(\tau_i) R^2(\tau_i) K_H(\tau_i, \tau_j) \frac{1}{2} W_\alpha(\tau_j) \quad i \neq j,$$

$$= \left\{ 1 - \sigma(\tau_i) B_H(\tau_i) R^2(\tau_i) \left[ \int K_H(\tau_i, \tau) d\tau - \sum_{i \neq j} K_H(\tau_i, \tau_j) \frac{1}{2} W_\alpha(\tau_j) \right] \right\} \quad i = j,$$

$$M_{HK}^{ij} = 0 \quad i \neq j,$$

$$= -2 B_{KH}(\tau_i) / B_K(\tau_i) \quad i = j,$$

$$M_{K}^{ij} = -\sigma(\tau_i) B_K(\tau_i) R^2(\tau_i) K_H(\tau_i, \tau_j) \frac{1}{2} W_\alpha(\tau_j) \quad i \neq j,$$

$$= \left\{ 1 - \sigma(\tau_i) B_K(\tau_i) R^2(\tau_i) \left[ \int K_K(\tau_i, \tau) d\tau - \sum_{i \neq j} K_K(\tau_i, \tau_j) \frac{1}{2} W_\alpha(\tau_j) \right] \right\} \quad i = j,$$

$$M_{KH}^{ij} = 0 \quad i \neq j,$$

$$= -2 B_{HK}(\tau_i) / B_H(\tau_i) \quad i = j,$$

$$S_K^i = S_K(\tau_i) - \frac{1}{2} S_H(\tau_i) B_{HK}(\tau_i) / B_H(\tau_i)$$

and  $S_H^i = S_H(\tau_i) - 2 S_K(\tau_i) B_{KH}(\tau_i) / B_K(\tau_i).$

Eliminating the H line radiation vector in (A8),

$$[\mathcal{E}_K] = [Q] [\mathcal{S}], \quad (A9)$$

where  $[Q] = \left[ 1 - [M_K]^{-1} [M_{KH}] [M_H]^{-1} [M_{HK}] \right]$   
 and  $[\mathcal{S}] = [M_K]^{-1} [S_K] - [M_K]^{-1} [M_{KH}] [M_H]^{-1} [S_H].$

$[\mathcal{E}_K]$  is found by substitution of (A9) into (A8).

Sensitivity to the dilution factor enters through the S and B coefficients, which are calculated from equations (7), (A3), (A5) and the absolute photometry in the lines. For a given  $\gamma$ , a grid of  $K(\tau_i, \tau_j, \tau_0, \gamma)$  covering the entire range of  $\tau_0$  appropriate for the stars in Table 1 can be calculated simultaneously.

### e) The Wings

Natural damping determines the width of the atomic line profile, since collision rates are much less than the radiative rate. For CaII, the total radiative decay rate from the  $^2P_{3/2}$  level corresponds

to a value of  $a = 1.25 \times 10^{-3}$  for a Doppler width of  $4 \text{ km s}^{-1}$ . Hence, when  $\tau_0$  exceeds  $10^4$ , the damping wings also scatter stellar continuum radiation, and the source function given by equation (7) must be supplemented. The additional radiation scattered is estimated by entering the CaII curve of growth for pure absorption at  $\tau_0 = 10^4$ , the equivalent width exceeds that for a value of  $a = 0$  by a factor of 3. If it is further assumed that all of this additional radiation is thermalized, and that escape at frequencies far from line center is not effective, then the effect of wing opacity on the populations of the metastable levels is overestimated. In the limit of detailed balance, this corresponds to a maximum factor of 3 in the populations. For a fixed observed ratio  $N_m/N_1$ ,  $d_0$  is not greater than  $\sqrt{3}$  times that calculated above. After accounting for escape in the wings, the effect is further reduced. Since  $\tau_0 \sim 10^3$  for most of the stars, the solution above should give accurate, quantitative estimates of  $d_0$ . A more careful treatment of these lines would also have to include the effects of inhomogeneities on the radiative transfer.

#### f) The Numerical Solution

Computations were made on the Yerkes Observatory IBM 1130 computer. The system (A8) is well-conditioned in the sense defined by Hummer and Ybicki (1967). The numerical solution matches the analytic solutions derived in various limiting cases, including both the optically thin limit and the case of detailed balance in the H and K lines. In the latter case, the transfer equation is replaced by the expression equating the local rates



of H and K emission and absorption,  $n'(\vec{r}) A_d^k(\vec{r}) = n^s(\vec{r}) E^{s'}$ . Substitution of this expression into the statistical equilibrium equations (A3) led to the expression used to determine the curve in Figure 10. A solution obtained numerically also agrees with that found for a two-level atom in the same model envelope, calculated by Magnan (1968) using a Monte Carlo technique. Finally, the total energy emitted by the shell in all lines is computed to be the same as the total stellar energy scattered by it, to within 1%.

Table 1

## The Program Stars

Star	BS	Sp Type	V	$M_V$	$M_{bol}$	$\log T_{eff}$	$\frac{R^*}{R_{\odot}}$	E(B-V)	$A_{HK}$	distance [3.5]- (pc) [11.0]	$\langle P \rangle$	$\langle  \Delta P  \rangle$	$I_K$	
$\rho$ Per	921	M4 II-III	3.4	-1.5	-4.0	3.48	200	0.05	0.25	95	0.09	0.1	0.08	4
119 CE Tau	1845	M2 <sup>Iab-Ib</sup> or Ib	4.4	-5.0	-6.6	3.54	410	0.37	1.85	400	0.05	1.2	0.26	2
$\alpha$ Ori	2061	M2:Ia-Ib	0.7	-5.8	-7.2	3.54	1080	0.18	0.90	200	1.04	0.3	0.08	3
6 BU Gem	2197	M1-M2 Ia-Iab	6.4	-6.5	-7.9	3.54	950	0.54	2.70	1260	1.69	2.1	0.18	
$\psi^1$ Aur	2289	K5-M0 Iab-Ib	4.8	-5.8	-7.0	3.56	570	0.23	1.15	1000	-0.40	0.5	0.16	2
$\alpha$ Sco	6134	M1.5: Iab	0.9	-5.8	-7.2	3.54	840	0.11	0.55	175	0.63			3
$\alpha^1$ Her	6406	M5Ib-II	3.1	-2.4	-5.7	3.45	420			125	0.37	0.1	.....	3
$\delta^2$ Lyr	7139	M4 II	4.3	-2.4	-4.9	3.48	310			220	0.21	0.1	.....	
R Lyr	7157	M4-5 III:	4.0	-0.5	-3.7	3.48	190	0.00	0.00	80	0.48	0.1	.....	
$\mu$ Cep	8316	M2:Ia	4.1	-6.5	-8.1	3.54	1030	0.55	2.75	1000	2.11	1.5	0.52	0
VV Cep	8383	M2 I comp.	4.9	-6.2	-7.8	3.54	900	0.04	0.20	1500	0.21			
$\beta$ Peg	8775	M2-M3 II-III	2.4	-1.5	-3.1	3.54	100	0.03	0.15	60	0.04	0.0	0.05	4
$\rho$ Cas	9045	G0:Ia	4.8	-8.4	-8.5	3.70	600	0.50	2.50	1900				

~~PRECEDING PAGE PLANE NOT FILMED~~

Notes to Table 1

- $\rho$  Per: Variable of class SRb, with a range in magnitude of 3.3 - 4.0v over a period of 40 days (Kukarkin 1969). Bobrovnikof has identified ZrO in spectra of moderate dispersion. Chromospheric Fe II emission is present below 3300Å (Bidelman and Pyper 1963).
- 119 Tau: Variable of class SRC, with a range of 6.1 - 6.5p over a period of 165 days. There is appreciable ZrO in the red, but these features are weaker than in  $\alpha$  Ori.
- $\alpha$  Ori: Variable of class SRC, with a range of 0.42 - 1.3v over a period of 2070 days. Superimposed on the main oscillation are waves with durations of several weeks to several months. The radial velocity is variable by about 10 km s<sup>-1</sup> on this time scale. The strength of ZrO  $\lambda$ 6473 is greater than in 119 Tau and  $\mu$  Cep. The Fe II emission lines below  $\lambda$ 3300Å arise in a chromosphere which is falling at a rate of 5 km s<sup>-1</sup> (Boesgaard and Magnan 1975). The angular diameter increases with decreasing wavelength (Bonneau and Labeyrie 1973), indicating limb darkening and possibly a large amount of scattering by dust. The radius is probably variable.
- 6 Gem: Variable of class Lc(?), with a range of 6.1 - 7.5v. This star is possibly an eclipsing variable with a period of 32 years. Ba II  $\lambda$ 4554 is not obviously strong at low dispersion. Stothers (1972) lists 6 Gem as a member of the I Gem association.

- $\psi^1$ Aur: Probable irregular variable (Lc?) with a range in magnitude of 6.6 - 7.2v. Ba II does not seem very strong at 40 A  $\text{mm}^{-1}$ .
- $\alpha$  Sco: Variable of class SRa, with a range of 0.88 - 1.8V over a period of 1733 days. The radial velocity is also variable. Ba II  $\lambda 4554$  is similar in strength to that of  $\alpha$  Ori; Boesgaard gives Ti/Zr greater than in  $\alpha$  Ori. Fe II emission is present. No hydrogen emission lines are present in the nebula surrounding the B star (Struve 1955). The companion has interstellar Ca II H and K absorption lines in its spectrum at a heliocentric velocity of  $-14.8 \text{ km s}^{-1}$ . The angular diameter of the primary is  $0.042 \pm 0.002$  arc sec (Gezari et al. 1972).  $\alpha$  Sco is a member of the Sco - Cent association.
- $\alpha^1$ Her: Variable of class SRc, with a range of 3.0 - 4.0v. Overlying a 6 year period with an amplitude of  $0^m.5$  are 50 - 130<sup>d</sup> fluctuations with amplitudes between 0.3 and  $1^m.0$ . The radial velocity is variable by 8 km/sec. There is no obvious evidence of ZrO. Fe II emission is more prominent than in  $\alpha$  Sco. The angular diameter is  $0.031 \pm 0.003$  arc sec. Knapp et al. (1975) recently redetermined the effective temperature to be  $2450^\circ \text{ K}$  on the basis of a new angular diameter measurement ( $0.058 \pm 0.009$  arc sec).
- $\delta^2$ Lyr: Variable (class not established) within the range 5.89 - 6.4B. Boesgaard<sup>(1970)</sup> gives normal M type abundance for Zr. Fe II emission is present.

R Lyr: Variable of class SRb, with a range of 3.9 - 5.0v over a period of 46 days. There is no obvious evidence for ZrO. Ca II H and K (Morgan and Keenan 1973) and Fe II are present in emission.

$\mu$  Cep: Variable of class SRC, with a range of 3.6 - 5.1v. Analyses of the light curve have led to several suggested periods, including proposed stochastic variability. The radial velocity varies over a range of 5 km s<sup>-1</sup>, in phase with the light variations; weak Balmer emission lines have been observed at maximum light (McLaughlin 1946). ZrO is very weak.  $\mu$  Cep is a probable member of the I Cep association (Johnson 1968).

W Cep: Variable of type EA (spectroscopic binary; period, 7430 days), with a range of 6.6 - 7.4p. The primary varies semiregularly with a period of 349 days and an amplitude of 0<sup>m</sup>.3. Superimposed is a slower oscillation with a period of 13.7 years and an amplitude of 0<sup>m</sup>.15. [Fe II] emission lines are present. There is no evidence of enhanced metal abundances. This system is a member of the II Cep association (Stothers 1972).

$\beta$  Peg: Variable of class Lb with a range of 2.3 - 2.8v. A1- (1970) though the ZrO  $\lambda$ 6473 feature is strong, Boesgaard lists the star as showing no evidence of enhanced ZrO. Fe II emission is present. The angular diameter is 0.016  $\pm$  0.002 arc sec.

$\rho$  Cas: Variable (RCB?) with a range 4.1 - 6.2v. No enhancement of the heavy metals has been reported.  $\rho$  Cas has undergone several major changes in spectral type since 1946 (Sargent 1961 and references). Fe II emission lines at  $\lambda$ 3669 and 3966 (multiplet 3) are present at the photospheric velocity.

Table 2

Symmetric Lines

Stars with known CS envelopes

U Del	M5 II-III	$\lambda$ 8542 symmetric
19 Psc	C6 <sub>2</sub>	$\lambda$ 8542 asymmetric

Stars with known CS envelopes and chromospheres

			I
			K
$\rho$ Per	M4 IIb-IIIa	$\lambda\lambda$ 4554, 4934, 7699 symmetric	4
$\alpha$ Ori	M2:Ia-Ib	$\lambda$ 6142 symmetric	3
$\pi$ Aur	M3 I	$\lambda$ 8542 symmetric	4
$\eta$ Gem	M3 III	$\lambda\lambda$ 4078, 7699 and 8542 symmetric; 5896 asymmetric	
g Her	M6-III	$\lambda$ 8542 symmetric, 7699 strongly asymmetric	
$\alpha^1$ Her	M5 Ib-II	$\lambda$ 4934 symmetric	3
$\delta^2$ Lyr	M4 II	$\lambda\lambda$ 4554, 4934 symmetric	
R Lyr	M4-5 III:	$\lambda\lambda$ 4554, 4934 symmetric	
$\epsilon$ Peg	K2 Ib	$\lambda\lambda$ 4078, 4554 and 8498 symmetric	4
		$\lambda\lambda$ 8542, 8662 variable	
$\beta$ Peg	M2.5 II III	$\lambda\lambda$ 4554, 4934 symmetric	4

Stars with known chromospheres

$\beta$ Cet	K1 III	$\lambda\lambda$ 8542, 8662, 8498 symmetric	2
$\beta$ And	M0 IIIa	$\lambda\lambda$ 8542, 8662, 8498 symmetric	4
$\alpha$ Tau	K5 III	$\lambda\lambda$ 8542, 8662, 8498 symmetric	4
$\iota$ Aur	K3 II	$\lambda$ 8662 symmetric	3
$\mu$ Gem	M3 IIIab	$\lambda$ 8542 symmetric	5
$\epsilon$ Gem	G8 Ib	$\lambda$ 8542 variable(?)	4
$\sigma^1$ CMa	K2.5 Iab	$\lambda\lambda$ 4554, 8542 symmetric	3
$\sigma$ CMa	K7 Ib	$\lambda$ 4554 symmetric, 8542 asymmetric	
$\mu$ UMa	M0 III	$\lambda$ 4554 symmetric	4
$\delta$ Vir	M3 III	$\lambda$ 8542 symmetric	2
$\xi$ Cyg	K4.5 Ib-II	$\lambda$ 8542 asymmetric, variable(?)	3

Table 3

Adopted Binary Data

System	Member	V	Separation (a.u.)	R/R <sub>o</sub>	M /M <sub>o</sub>
VV Cep	M2 I	4.9		900	80
	B1 V	8.10	45	24	40
$\alpha$ Sco	M1.5:Iab	0.9		840	
	B4 V	5.04	500	4	
$\alpha^1$ Her	M5 Ib-II	3.1		420	
	G0 II-III	5.16	600	12	
	A3V?	7.26	600	1.7	



Table 4

Photospheric				Photospheric (continued)			
$\lambda$ (Å)	Iden.	Int.	$\Delta V$ (km s <sup>-1</sup> )	$\lambda$ (Å)	Iden.	Int.	$\Delta V$ (km s <sup>-1</sup> )
4076.887	FeI 557	12	-62.31	4554.460	FeI 319	{15}	27.93
4077.072	CrI 66	{ 9 }	-47.97	4554.536	RuI 5		32.94
4077.148	TiI 207		-42.38	4555.069	TiI 266	10	68.05
4077.347	LaII 41 YI 7	16	-27.74	4933.338	FeI 1065	13	-46.03
4077.724	SrII 1	40	00.00	4934.030	FeI 1068	{ 40 }	-3.95
4077.969	DyII	20	18.02	4934.095	BaII 1		
4078.321	CeII 19	{ 16 }	43.92	4934.59	TiO	5	30.10
4078.365	FeI 217		47.16	4934.95	TiO	5	52.90
4078.444	GdII 15		52.97	5888.81	TiO	4	-59.23
4215.023	GdII 32	6	-35.66	5889.973	NaI 1	90	00.00
4215.170	CN(0,1)P <sub>30</sub> <sup>15</sup>		-26.26	5891.12	FeI 581		58.42
4215.297	CN(0,1)P29		-17.22	5891.35	TiO	6	70.13
4215.539	SrII 1	45	00.00	5895.05	TiO	0	-45.28
4215.976	FeI 273	4	31.10	5895.940	NaI 1	90	00.00
4216.191	FeI 3	43	46.40	5896.52	TiO	3	29.51
4553.01	Zr I 31	{ 11 }	-67.59	7698.22	TiO	9	-29.50
4553.056	VI 133		-64.56	7698.977	KI 1	30	00.00
4553.40	TiO	4	-41.70	7699.64	TiO	8	25.84
4554.036	BaII 1	37	00.00	7700.39	TiO	4	55.06

Photospheric(continued)

$\lambda$ (Å)	Iden.	Int.	$\Delta V$ (km s <sup>-1</sup> )
8496.994	FeI 1172	3	-37.70
8498.062	CaII 2	75	00.00
8498.44	Zr 40		13.34
8661.97	FeI 60		-69.26
8662.170	CaII 2	90	00.00

Telluric

5888.703	H <sub>2</sub> O	10	-64.68
5889.085	H <sub>2</sub> O	3	-45.23
5889.637	H <sub>2</sub> O	14	-17.11
5891.500	Atm	6	77.77
5891.660	H <sub>2</sub> O	18	85.92
5894.385	H <sub>2</sub> O	5	-79.12
5894.604	Atm	2.5	-67.98
5894.944	H <sub>2</sub> O	8.5	-50.68
5895.140	H <sub>2</sub> O	5.5	-40.70
5896.294	H <sub>2</sub> O	5	18.01
5896.418	H <sub>2</sub> O	18	24.32
5896.492	H <sub>2</sub> O		28.09
5896.832	H <sub>2</sub> O	10	45.38

Telluric(continued)

$\lambda$ (Å)	Iden.	Int.	$\Delta V$ (km s <sup>-1</sup> )
5897.461	H <sub>2</sub> O	7.5	77.39
7663.726	O <sub>2</sub>	5	-44.85
7663.90	O <sub>2</sub>	1	-37.97
7664.872	O <sub>2</sub>		00.00
7665.944	O <sub>2</sub>	468	41.96
7696.869	O <sub>2</sub>	57	-82.15
7696.996	O <sub>2</sub>	2	-77.20
7698.322	O <sub>2</sub>	4	-25.53
7699.506	O <sub>2</sub>	3	20.62
7701.078	O <sub>2</sub>	3	81.88
8499.885	H <sub>2</sub> O	6	+64.28
8539.888	H <sub>2</sub> O	3.5	-79.23
8540.817	H <sub>2</sub> O	8	-46.60

Table 5

## Adopted Atomic Constants

Atom	Abundance (H=1)	Transition	$\lambda$ (Å)	$\omega_{LFLU}$	$\Lambda_{UL}$ (s <sup>-1</sup> )
CaII	1.66x10 <sup>-6</sup>	1-5 $^2S_{1/2} - ^2P_{3/2}$	3934	1.33	1.5x10 <sup>8</sup>
		1-4 $^2S_{1/2} - ^2P_{1/2}$	3968	0.67	1.4x10 <sup>8</sup>
		3-5 $^2D_{5/2} - ^2P_{3/2}$	8542	0.54	1.2x10 <sup>7</sup>
		2-5 $^2D_{3/2} - ^2P_{3/2}$	8662	0.30	1.3x10 <sup>7</sup>
		2-4 $^2D_{3/2} - ^2P_{1/2}$	8498	0.06	1.4x10 <sup>6</sup>
		1-3 $^2S_{1/2} - ^2D_{3/2}$	7291		1.3
		1-2 $^2S_{1/2} - ^2D_{1/2}$	7324		1.3
SrII	5.62x10 <sup>-10</sup>	$^2S_{1/2} - ^2P_{3/2}$	4078	1.25	1.3x10 <sup>8</sup>
		$^2S_{1/2} - ^2P_{1/2}$	4216	0.62	1.2x10 <sup>8</sup>
		$^2D_{5/2} - ^2P_{3/2}$	10327	0.46	7 x10 <sup>6</sup>
BaII	1.23x10 <sup>-10</sup>	$^2S_{1/2} - ^2P_{3/2}$	4554	1.33	1.1x10 <sup>8</sup>
		$^2S_{1/2} - ^2P_{1/2}$	4934	0.67	9 x10 <sup>7</sup>
		$^2D_{5/2} - ^2P_{3/2}$	6142	0.50	2 x10 <sup>7</sup>
NaI	1.66x10 <sup>-6</sup>	$^2S_{1/2} - ^2P_{3/2}$	5890	1.31	6.2x10 <sup>7</sup>
		$^2S_{1/2} - ^2P_{1/2}$	5896	0.65	6.2x10 <sup>7</sup>
KI	7.59x10 <sup>-8</sup>	$^2S_{1/2} - ^2P_{3/2}$	7665	1.32	3.7x10 <sup>7</sup>
		$^2S_{1/2} - ^2P_{1/2}$	7699	0.66	3.7x10 <sup>7</sup>

Table 6

Column Densities and Kinematics\*

Star	$\lambda$	$\gamma = 0.5$			$\gamma = 1.0$			$\gamma = 1.35$			$\gamma = 2.0$		
		$\tau_o$	$V_e$	N	$\tau_o$	$V_e$	N	$\tau_o$	$V_e$	N	$\tau_o$	$V_e$	N
$\rho$ Per	4078	0.50	3.1	8.2 <sup>11</sup>	0.27	5.3	3.7 <sup>11</sup>	0.25	5.8	2.8 <sup>11</sup>	0.20	6.0	1.6 <sup>11</sup>
	4216	0.42	4.6	2.0 <sup>12</sup>	0.24	7.6	9.3 <sup>11</sup>	0.20	8.3	6.3 <sup>11</sup>	0.17	8.5	3.7 <sup>11</sup>
	5896				5.91	5.5	8.0 <sup>12</sup>	3.59	6.6	4.5 <sup>12</sup>	2.38	7.5	2.4 <sup>12</sup>
	8542	0.50	4.2	3.6 <sup>12</sup>	0.26	7.1	1.6 <sup>12</sup>	0.23	7.7	1.1 <sup>12</sup>	0.18	7.9	6.2 <sup>11</sup>
119 Tau	4554	2.80	3.7	4.5 <sup>12</sup>	1.05	6.9	1.6 <sup>12</sup>	0.86	7.8	1.1 <sup>12</sup>	0.73	9.0	7.2 <sup>11</sup>
	4934	1.00	4.7	3.9 <sup>12</sup>	0.48	7.6	1.5 <sup>12</sup>	0.42	8.5	1.1 <sup>12</sup>	0.36	9.1	6.7 <sup>11</sup>
	7699				7.10	5.3	9.9 <sup>12</sup>	4.06	6.7	5.3 <sup>12</sup>	2.60	8.0	2.8 <sup>12</sup>
	8542	1.42	5.4	1.3 <sup>13</sup>	0.71	9.5	5.9 <sup>12</sup>	0.62	10.7	4.3 <sup>12</sup>	0.47	11.9	2.4 <sup>12</sup>
	8662	1.26	5.4	1.4 <sup>13</sup>	0.60	9.5	5.9 <sup>12</sup>	0.52	10.7	4.2 <sup>12</sup>	0.83	11.7	5.0 <sup>12</sup>
$\alpha$ Ori	4554	0.87	2.7	1.0 <sup>12</sup>	0.52	4.6	4.3 <sup>11</sup>	0.43	5.1	3.1 <sup>11</sup>	0.32	5.4	1.9 <sup>11</sup>
	4934	0.21	3.8	3.9 <sup>11</sup>	0.43	6.2	3.3 <sup>11</sup>	0.37	6.6	2.4 <sup>11</sup>	0.10	6.6	1.3 <sup>11</sup>
	7699							$\lambda 20$	5.6	$\lambda 2.2^{13}$	5.13	8.1	5.5 <sup>12</sup>
	8542	0.55	5.1	4.9 <sup>12</sup>	0.13	8.7	2.3 <sup>12</sup>	0.12	9.5	1.7 <sup>12</sup>	0.23	9.9	9.9 <sup>11</sup>
6 Gem	4934	1.63	4.9	6.6 <sup>12</sup>	0.72	8.7	2.6 <sup>12</sup>	0.60	9.9	1.8 <sup>12</sup>	0.52	11.0	1.2 <sup>12</sup>
	7699						$\lambda 20$	4.9	$\lambda 1.9^{13}$	6.80	6.8	6.1 <sup>12</sup>	
	8542	2.00	7.3	2.5 <sup>13</sup>	0.89	13.1	1.0 <sup>13</sup>	0.74	14.8	7.1 <sup>12</sup>	0.63	16.8	4.6 <sup>12</sup>
$\psi^1$ Aur	4554	1.33	4.4	2.6 <sup>12</sup>	0.62	7.7	1.0 <sup>12</sup>	0.53	8.7	7.5 <sup>11</sup>	0.36	9.5	3.7 <sup>11</sup>
	7699				5.50	8.6	1.3 <sup>13</sup>	3.36	6.0	3.9 <sup>12</sup>	2.28	7.1	2.1 <sup>12</sup>
	8542	6.15	5.5	5.9 <sup>13</sup>	1.80	11.2	1.8 <sup>13</sup>	1.38	13.1	1.2 <sup>13</sup>	1.17	15.8	8.1 <sup>12</sup>
	8662	3.70	5.5	4.2 <sup>13</sup>	1.26	10.5	1.4 <sup>13</sup>	1.03	12.0	9.4 <sup>12</sup>	0.87	14.0	6.3 <sup>12</sup>
$\alpha$ Sco	4552	0.21	5.2	4.8 <sup>11</sup>	0.13	8.6	2.4 <sup>11</sup>	0.12	9.1	1.8 <sup>11</sup>	0.10	9.0	9.9 <sup>10</sup>
	4934	0.12	3.0	3.0 <sup>11</sup>	0.08	5.0	1.6 <sup>11</sup>	0.06	5.3	9.6 <sup>10</sup>	0.07	5.1	7.5 <sup>10</sup>
	7699	3.15	5.3	8.7 <sup>12</sup>	1.13	9.9	3.0 <sup>12</sup>	0.93	11.3	2.1 <sup>12</sup>	0.78	12.6	1.3 <sup>12</sup>
	8498	1.12	4.3	5.1 <sup>13</sup>	0.54	7.6	2.2 <sup>13</sup>	0.42	8.6	1.4 <sup>13</sup>	0.39	9.2	9.4 <sup>12</sup>
	8542	2.33	5.0	2.0 <sup>13</sup>	0.93	9.1	7.4 <sup>12</sup>	0.72	10.5	4.9 <sup>12</sup>	0.65	11.9	3.4 <sup>12</sup>
	8662	2.33	5.9	2.8 <sup>13</sup>	0.93	10.8	1.0 <sup>13</sup>	0.72	12.4	6.8 <sup>12</sup>	0.65	14.0	4.7 <sup>12</sup>

\* The entry 8.2<sup>11</sup> for N means  $N=8.3 \times 10^{11} \text{ cm}^{-2}$ ; the units of  $V_e$  are  $\text{km s}^{-1}$ .

Table 6 (continued)

Star	$\lambda$	$\gamma = 0.5$			$\gamma = 1.0$			$\gamma = 1.35$			$\gamma = 2.0$		
		$\tau_0$	$V_e$	N	$\tau_0$	$V_e$	N	$\tau_0$	$V_e$	N	$\tau_0$	$V_e$	N
$\alpha^1$ Her	4216	2.48	2.9	$7.3^{12}$	0.97	5.3	$2.6^{12}$	0.80	6.0	$1.8^{12}$	0.68	6.9	$1.2^{12}$
	4554	0.50	5.7	$1.3^{12}$	0.27	9.7	$5.8^{11}$	0.25	10.4	$4.2^{11}$	0.20	10.8	$2.4^{11}$
	7699				$\approx 20$	$\approx 5.3$	$\approx 2.8^{13}$	6.10	6.9	$8.2^{12}$	3.56	8.6	$4.0^{12}$
	8542	1.06	3.7	$6.9^{12}$	0.52	6.5	$3.0^{12}$	0.43	7.4	$2.0^{12}$	0.38	7.9	$1.3^{12}$
	8662	0.55	4.2	$4.8^{12}$	0.30	7.2	$2.2^{12}$	0.27	7.9	$1.6^{12}$	0.22	8.2	$9.3^{11}$
$\delta^2$ Lyr	4078	2.48	4.2	$5.4^{12}$	0.97	7.7	$1.9^{12}$	0.80	9.5	$1.5^{12}$	0.68	10.0	$8.8^{11}$
	4216	0.60	2.7	$1.6^{12}$	0.33	4.5	$7.6^{11}$	0.28	5.0	$5.4^{11}$	0.23	5.2	$3.1^{11}$
	5890				2.33	6.0	$2.4^{12}$	1.73	7.0	$1.5^{12}$	1.38	8.1	$9.6^{11}$
	5896				2.60	6.3	$5.6^{12}$	1.85	7.4	$3.5^{12}$	1.48	8.6	$2.2^{12}$
	8542	1.00	5.7	$9.9^{12}$	0.48	9.0	$3.8^{12}$	0.42	10.2	$2.8^{12}$	0.36	10.9	$1.7^{12}$
R Lyr	4078	1.06	3.4	$1.9^{12}$	0.52	5.9	$8.0^{11}$	0.43	6.6	$5.5^{11}$	0.38	7.1	$3.5^{11}$
	4216	0.35	4.9	$1.8^{12}$	0.20	8.2	$8.4^{11}$	0.17	8.8	$5.7^{11}$	0.17	9.0	$3.9^{11}$
	5890				3.12	5.1	$2.3^{12}$	2.10	6.1	$1.6^{12}$	1.63	7.0	$9.9^{11}$
	5896				7.10	3.5	$8.6^{12}$	4.05	4.4	$4.5^{12}$	2.62	5.4	$2.4^{12}$
	8542	0.27	3.1	$1.5^{12}$	0.17	5.1	$7.5^{11}$	0.15	5.5	$5.4^{11}$	0.13	5.5	$3.1^{11}$
$\mu$ Cep	4554	0.70	4.5	$1.4^{12}$	0.36	7.8	$6.1^{11}$	0.32	8.6	$4.5^{11}$	0.27	9.0	$2.7^{11}$
	7699	2.63	4.1	$6.3^{12}$	1.00	8.6	$2.3^{12}$	0.83	9.7	$1.6^{12}$	0.70	10.1	$9.3^{11}$
	8542	0.65	4.0	$4.5^{12}$	0.34	6.8	$2.0^{12}$	0.30	7.5	$1.5^{12}$	0.25	7.9	$8.6^{11}$
VV Cep	4554	0.27	4.0	$4.7^{11}$	0.17	6.5	$2.4^{11}$	0.15	7.0	$1.7^{11}$	0.13	7.0	$1.0^{11}$
	7699	0.35	3.6	$\approx 6.7^{11}$	0.20	6.1	$\approx 3.2^{11}$	0.17	6.4	$\approx 2.6^{11}$	0.15	6.8	$\approx 1.3^{11}$
	8542	0.82	6.8	$9.6^{12}$	0.41	11.7	$4.2^{12}$	0.36	13.1	$3.0^{12}$	0.30	13.8	$\approx 1.8^{12}$
$\beta$ Peg	4078	0.15	2.9	$2.3^{11}$	0.10	4.8	$1.3^{11}$	0.08	5.1	$7.8^{10}$	0.07	7.9	$6.2^{11}$
	4216	0.15	3.6	$5.6^{11}$	0.10	6.0	$3.1^{11}$	0.08	6.3	$1.9^{11}$	0.07	6.2	$1.1^{11}$
	5890				4.63	4.4	$3.5^{12}$	2.86	4.0	$2.0^{12}$	2.02	6.3	$1.1^{12}$
	5896				3.75	5.0	$6.4^{12}$	2.42	4.5	$3.7^{12}$	1.80	7.4	$1.7^{12}$
	7699										0.08	11.3	$\approx 1.6^{11}$
	8542	0.27	3.7	$1.8^{12}$	0.17	6.2	$9.2^{11}$	0.15	6.8	$6.6^{11}$	0.13	6.7	$\approx 3.8^{11}$

Table 6 (continued)

Star	$\lambda$	$\gamma = 0.5$			$\gamma = 1.0$			$\gamma = 1.35$			$\gamma = 2.0$		
		$\tau_0$	$V_e$	N	$\tau_0$	$V_e$	N	$\tau_0$	$V_e$	N	$\tau_0$	$V_e$	N
$\rho$ Cas	4554							~9	21.1	~3.1 <sup>13</sup>	4.00	27.8	1.2 <sup>13</sup>
	4934							4.80	24.1	3.5 <sup>13</sup>	2.95	29.5	1.8 <sup>13</sup>
	7699				2.46	13.5	8.8 <sup>12</sup>	1.78	16.0	5.5 <sup>12</sup>	1.42	18.9	3.7 <sup>12</sup>
	8498				0.96	15.5	7.8 <sup>13</sup>	0.80	17.6	5.4 <sup>13</sup>	0.65	19.6	3.3 <sup>13</sup>
	8542				1.25	15.5	1.7 <sup>13</sup>	1.03	17.8	1.2 <sup>13</sup>	0.83	19.9	7.2 <sup>12</sup>

Table 7

## Shell Properties \*

Star	$\Gamma_K/\alpha$	$\gamma=0.5$				$\gamma=1.0$			
		$x_0$	$n_H$	$n_e/n_H$	$\dot{M}$	$x_0$	$n_H$	$n_e/n_H$	$\dot{M}$
$\rho$ Per	1.4	3.2	5.6		2.0	3.4	2.5	0.73	1.7
119 Tau	2.4	3.1	37		55	2.8	15	1.1	33
$\alpha$ Ori	2.5	3.7	2.0		22	4.0	1.0		23
6 Gem	0.68	5.1	15		380	5.0	6.1		270
$\psi^1$ Aur	5.4	4.0	13		64	4.9	4.2	7.9	57
$\alpha$ Sco	$3.3 \times 10^3$	3.7	1.4	$9.0 \times 10^4$	12	4.7	0.56	$4.8 \times 10^4$	13
$\alpha^1$ Her	0.45	2.4	16		16	2.2	0.72	7.3	10
$\delta^2$ Lyr	2.7	3.0	9.6		3.6	3.1	3.6	0.21	4.5
R Lyr	0.62	3.4	7.2		2.8	3.1	3.6	0.15	2.0
$\mu$ Cep	2.9	10.5	1.4	5.0	160	10.5	0.62	1.8	130
VV Cep	$7.6 \times 10^6$	4.8	1.2	$9.0 \times 10^6$	20	5.5	0.55	$7.3 \times 10^6$	20
$\beta$ Peg	5.4	2.7	3.6		0.20	2.9	1.9		0.20
$\rho$ Cas	17								

\* Units:  $\Gamma_K/\alpha$  in  $10^4 \text{ cm}^{-3}$  $n_e/n_H$  in  $10^{-7}$  $n_H$  in  $10^7 \text{ cm}^{-3}$  $\dot{M}$  in  $10^{-8} M_\odot \text{ yr}^{-1}$

Table 7 (continued)

Star	$\gamma=1.35$				$\gamma=2.00$			
	$x_0$	$n_H$	$n_e/n_H$	$\dot{M}$	$x_0$	$n_H$	$n_e/n_H$	$\dot{M}$
$\rho$ Per	3.4	1.7	0.59	1.2	3.4	0.99	0.54	0.74
119 Tau	2.7	11	1.2	24	2.5	7.6	1.1	16
$\alpha$ Ori	4.0	0.72	$\approx 150$	17	3.9	0.43	64	10
6 Gem	5.1	4.2	$\approx 0.56$	210	5.1	2.7	0.28	160
$\psi^1$ Aur	5.2	2.8	3.1	48	4.1	1.8	4.3	21
$\alpha$ Sco	4.9	0.37	$4.8 \times 10^4$	10	4.7	0.23	$5.2 \times 10^4$	5.7
$\alpha^1$ Her	2.3	4.9	2.9	8.2	2.2	3.1	3.3	5.1
$\delta^2$ Lyr	3.6	2.9	0.12	4.8	3.5	1.8	0.12	2.8
R Lyr	3.1	2.4	0.13	1.4	3.3	1.5	0.097	1.1
$\mu$ Cep	10.5	0.47	1.7	100	10.5	0.39	1.7	70
VV Cep	5.5	0.38	$\approx 8.4 \times 10^6$	13	5.4	0.23	$\approx 7.6 \times 10^6$	8.5
$\beta$ Peg	2.4	1.4		0.11	2.5	0.78	$\approx 48$	0.081
$\rho$ Cas	>1	<620	0.037	1200	>1	<280	0.12	680



Table 8

Multiple Absorption Components in the  
NaI and KI Resonance Lines

Star	$\lambda$ (Å)	Heliocentric Velocity (km s <sup>-1</sup> )	$V_{CS} - V_{*}$ (km s <sup>-1</sup> )	Description*		
$\alpha$ Ori	7699	+13	-10	strong, wide		
		+ 6	-17	weak, narrow		
$\alpha$ Sco	5890	- 6	- 6	weak, narrow (IS?)		
		-18	-18	strong, wide (IS?)		
	5896	- 6	- 6	weak, narrow (IS?)		
		-17	-17	strong, wide (IS?)		
7699	- 5	- 5	weak, narrow (IS?)			
	-12	-12	strong (IS?)			
	-18	-18	strong, wide (IS?)			
$\alpha^1$ Her	7699	-48	-13	strong, wide		
		-52	-18	weak, narrow		
$\mu$ Cep	7665	+13	-12	strong		
		+ 5?	-20	blended with telluric O <sub>2</sub>		
		-12	-37	strong, narrow (IS?)		
		-18	-43	narrow (IS?)		
		-26	-51	blended with -18 km s <sup>-1</sup> component		
		7699	+12	-13	strong, wide	
			+ 5	-20	weak, narrow (IS?)	
				-11	-36	very weak (IS?)
				-13	-38	narrow (IS?)
				-18	-43	strong (IS?)
		-27	-52	narrow		
VV Cep	7699	-17	+15	IS		
$\beta$ Peg	5890	- 2	-10	strong, narrow (IS?)		
		5896	- 2	-10	strong, narrow (IS?)	
	7699	- 4	-12	weak, narrow (IS?)		
$\rho$ Cas	7699	-15	+33	IS		

\* IS denotes interstellar.

REFERENCES

- Adams, W. S. and McCormack, E. 1935, Ap. J., 81, 119.
- Allen, C. W. 1973, Astrophysical Quantities (London: Athlone Press).
- Bahcall, J. N. and Wolf, R. A. 1968, Ap. J., 152, 701.
- Bidelman, W. P. and McKellar, A. 1957, Pub. A.S.P., 69, 31.
- Bidelman, W. P. and Pyper, D. M. 1963, Pub. A.S.P., 75, 389.
- Blanco, V. M. 1965, in Stars and Stellar Systems, Vol. 5, ed. A. Blaauw and M. Schmidt (Chicago: University of Chicago Press), p. 241.
- Boesgaard, A. M. 1970, Ap. J., 161, 163.
- Boesgaard, A. M. and Magnan, C. 1975, Ap. J., 198, 369.
- Bonneau, D. and Labeyrie, A. 1973, Ap. J. (Letters), 181, L1.
- Burbidge, E. M. and Burbidge, G. R. 1957, Ap. J., 126, 357.
- Burgess, A., Field, G. B., and Michie, R. W. 1960, Ap. J., 131, 529.
- Capriotti, E. R. 1964, Ap. J., 139, 225.
- Cowley, A. P. 1969, Pub. A.S.P., 81, 297.
- Davis, D. N. 1946, Ap. J., 106, 28.
- Deutsch, A. J. 1956, Ap. J., 123, 210.
- \_\_\_\_\_. 1960, in Stars and Stellar Systems, Vol. 6, ed. J. L. Greenstein (Chicago: University of Chicago Press), p. 543.
- \_\_\_\_\_. 1968, in Mass Loss from Stars, ed. M. Hack (New York: Springer-Verlag; Dordrecht: D. Reidel Publishing Co.).
- Doherty, L. R. 1972a, Ap. J., 178, 495.
- Doherty, L. R. 1972b, Ap. J., 178, 727.
- Dyck, H. M. and Johnson, H. R. 1969, Ap. J., 156, 389.
- Dyck, H. M., Forrest, W. J., Gillett, F. G., Stein, W. A., Gehrz, R. D., Woolf, N. J. and Shawl, S. J. 1971, Ap. J., 165, 57.

- Evans, D. C. 1972, Scientific Results from OAO-2, NASA SP-310, ed. A. D. Code, p. 347.
- Fix, J. D. and Alexander, D. R. 1974, Ap. J. (Letters), 188, L91.
- Gezari, D. Y., Labeyrie, A. and Stachnik, R. V., 1972, Ap. J. (Letters), 173, L1.
- Gehrz, R. D. and Woolf, N. J. 1971, Ap. J., 165, 285.
- Gillett, F. C., Hyland, A. R. and Stein, W. A. 1970, Ap. J. (Letters), 162, L21.
- Goldberg, L., Ramsey, L., Testerman, L. and Carbon, D. 1975, Ap. J., 199, 427.
- Herzberg, G., 1948, Ap. J., 107, 94.
- Hobbs, L. M. 1974, Ap. J., 191, 385.
- Hudson, R. D. 1964, Phys. Rev. A, 135, 1212.
- Hudson, R. D. and Carter, V. L. 1965, Phys. Rev. A, 139, 1426.
- Hummer, D. G. and Rybicki, G. 1967, in Methods in Computational Physics, Vol. 7, ed. B. Alder, S. Fernbach and M. Rotenberg (New York: Academic Press), p. 53.
- Jennings, M. C. and Dyck, H. M. 1972, Ap. J., 177, 427.
- Johnson, H. L. 1968, in Stars and Stellar Systems, Vol. 7, ed. B. M. Middlehurst and L. H. Aller (Chicago: University of Chicago Press), p. 167.
- Johnson, H. L., Mitchell, R. I., Iriarte, B., and Wisniewski, W. Z. 1966, Comm. Lunar and Planet. Lab., 4, 99.
- Knapp, S. L., Currie, D. G. and Liewer, K. M. 1975, Ap. J., 198, 561.
- Kukarkin, B. V. 1969, General Catalogue of Variable Stars (3d ed.; Moscow: Astronomical Council of the Academy of Sciences of the USSR).

- Lee, T. A. 1970, Ap. J., 162, 217.
- Magnan, C. 1968, Astrophysical Letters, 2, 213.
- McLaughlin, D. B. 1946, Ap. J., 103, 35.
- Mihalas, D. 1973, Ap. J., 179, 209.
- Moore, C. E., Minnaert, M. G. J., and Houtgast, J. 1966, The Solar Spectrum 2935 to 8770Å, NBS Monograph 61, (Washington: U.S. Government Printing Office).
- Morgan, W. W. and Keenan, P. C. 1973, Ann. Rev. Astr. and Ap., 3, 29.
- Osterbrock, D. E. 1973, 18th Liège Astrophys. Symposium, V:391.
- Quirk, W. J. and Tinsley, B. M. 1973, Ap. J., 179, 69.
- Reimers, D. 1975, in Problems in Stellar Atmospheres and Envelopes, ed. B. Baschek, W. H. Hegel, and G. Traving (New York: Springer-Verlag).
- Robbins, R. R. 1968, Ap. J., 151, 511.
- Rood, R. T. 1973, Ap. J., 184, 815.
- Sargent, W. L. W. 1961, Ap. J., 134, 142.
- Sargent, W. L. W. and Osmer, P. S. 1969, in Mass Loss from Stars, ed. M. Hack (New York: Springer-Verlag; Dordrecht: D. Reidel Publishing Co.).
- Seaton, M. J. 1951, M.N.R.A.S., 111, 368.
- Schmidt, M. 1959, Ap. J., 129, 243.
- Schwartz, P. R. and Barrett, A. H. 1970, Ap. J. (Letters), 159, L123.
- Schwarzschild, M. 1961, Transactions of the I.A.U., Vol. 11B, 137.
- Stothers, R. 1972, Pub. A.S.P., 84, 373.

- Straizys, V. and Sviderskiene, Z. 1972, Bulletin of the Vilnius Observatory, No. 35.
- Struve, O. 1955, Mem. Soc. Roy. Sci. Liège, 4th Ser., 20, 436.
- Underhill, A. B. 1972, Scientific Results from OAO-2, NASA SP-310, ed. A. D. Code, p. 367.
- Weymann, R. 1962, Ap. J., 136, 844.
- Weymann, R. 1963, Ann. Rev. Astr. and Ap., 1, 97.
- Wickramasinghe, N. C. Donn, B. D. and Stecher, T. P. 1966, Ap. J., 146, 590.
- Wilson, O. C. 1960, Ap. J., 132, 136.
- Wilson, O. C. and Bappu, M. K. 1957, Ap. J., 125, 661.
- Wilson, W. J., Barrett, A. H. and Moran, J. M. 1970, Ap. J., 160, 545.
- Wolf, N. J. and Ney, E. P. 1969, Ap. J. (Letters), 155, L181.

FIGURE CAPTIONS

- Fig. 1. Scans of the program lines. In boxes with more than one scan, tick marks on the upper and lower scales identify features in the scans plotted with open and solid figures, respectively. Solid lines on the velocity axes give the positions of stellar photospheric lines; dotted lines identify telluric features (Table 4). Possible interstellar features are listed in Table 8. In the barium and strontium scans, the upper and lower zero points refer to the scans plotted in open and solid figures, respectively. For the supergiants, high resolution scans of KI  $\lambda 7699$  (filled circles) are superimposed on lower resolution scans of the same line (open circles). In the scans of  $\alpha$  Sco and VV Cep, the dashed horizontal line gives an estimate of the contribution of the binary companion.
- Fig. 2. The strontium lines of the giant stars.
- Fig. 3. Representative scans showing the adopted stellar continuum.
- Fig. 4. Computed "metal" line profiles (filled circles) for  $\gamma=1.35$  and various choices of  $\tau_0$ . The open circles show the portion of the continuum which is redistributed.
- Fig. 5. Minimum residual intensity of the computed line profiles, plotted against optical depth at line center for various choices of  $\gamma$ . The interstellar (IS) case gives the limit in which there is no reemission along the line of sight in the line core.
- Fig. 6. The observed CS profile of Ba II  $\lambda 4934$  in  $\delta$  Gem (filled

circles) and several fits with theoretical profiles. The dashed profiles are drawn as in Figure 4. Ticks on the abscissa indicate the corresponding zero-velocity points in the coordinate system at rest with the shell's center of mass. The velocity range of the observed profile is  $45 \text{ km s}^{-1}$ .

Fig. 7. Column density  $N_{\text{II}}$  of the envelopes, in units of  $\text{cm}^{-2}$ , plotted against  $M_V$ , for the  $\gamma=1.35$  models. Lines connect estimates based on doublet pairs.

Fig. 8. Expansion velocity inferred from the line profiles, in  $\text{km s}^{-1}$ , plotted against  $M_V$ , for the  $\gamma=1.35$  models.

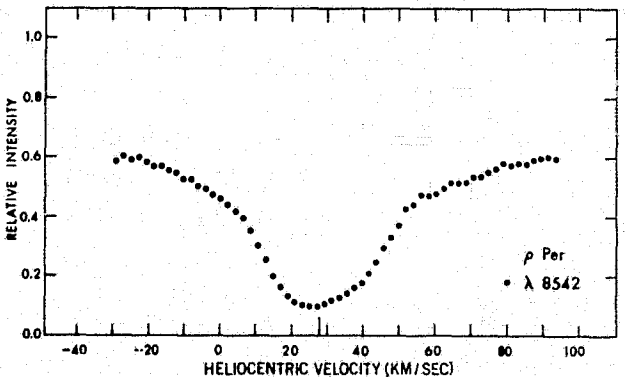
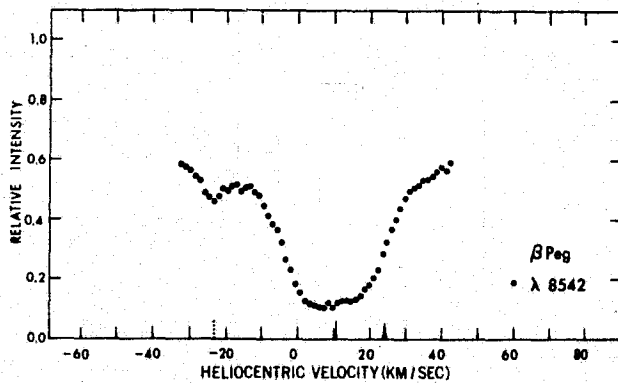
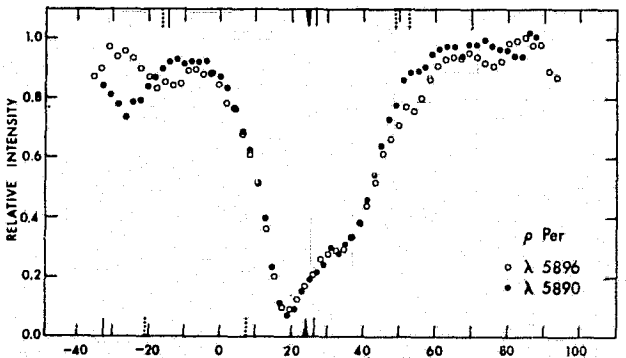
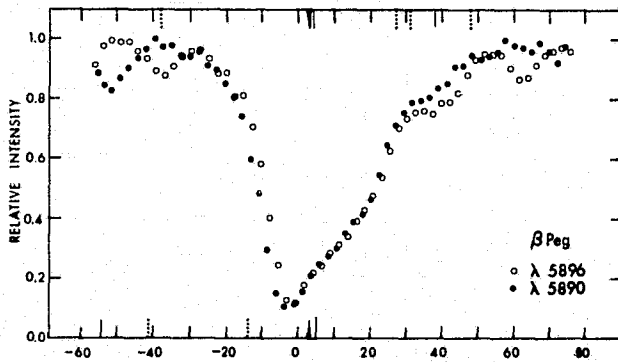
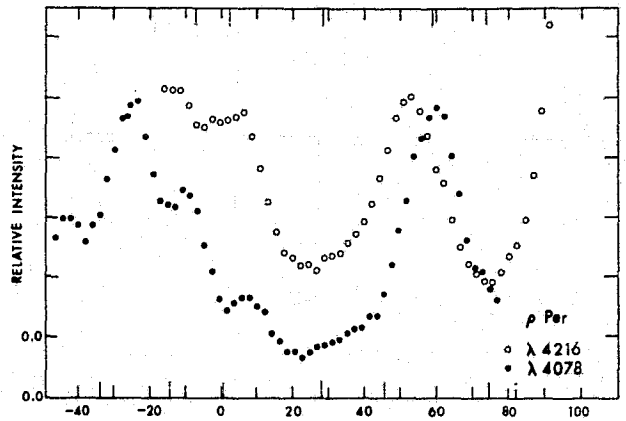
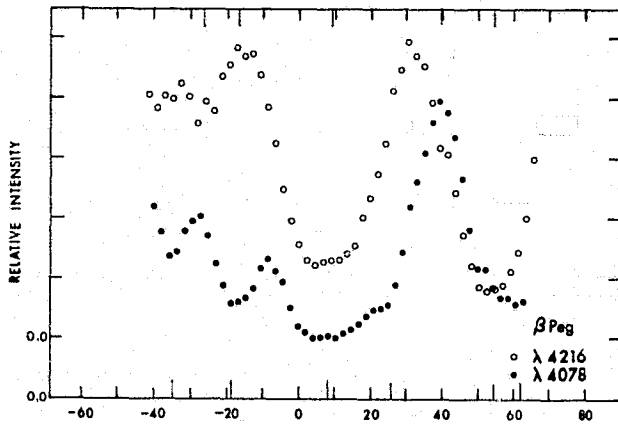
Fig. 9. Representative high resolution scans showing fine structure.

Fig.10. The computed ratio  $N_m/N_1$  of the  $^2D_{5/2}$  (heavy solid line) and  $^2D_{3/2}$  (heavy dashed line) levels of Ca II relative to the total Ca II column density, for R Lyr. The corresponding light lines give the solutions under the assumption of detailed balance in the H and K lines. The arrow on the ordinate indicates the value for the  $^2D_{5/2}$  level obtained from the data.

Fig.11. The mass loss rate, in units of  $M_\odot \text{ yr}^{-1}$ , plotted against  $M_V$ . Bars indicate the range of computed values based on various combinations of the metal and triplet line column densities. Arrows indicate lower limits for  $\rho \text{ Cas}$ ,  $\text{VV Cep}$  and  $\alpha \text{ Sco}$ . The least squares linear fit to the  $\gamma=1.35$  models for all the stars, excluding  $\text{VV Cep}$  and  $\alpha \text{ Sco}$ , is  $\log \dot{M} = -0.38(\pm 0.05)M_V - 8.6(\pm 0.2)$ .

Fig.12. Mass-loss rate, in units of  $M_\odot \text{ yr}^{-1}$ , plotted against intensity of the Ca II K-line chromospheric emission (Wilson and Bappu 1957).

Figure 1



PRECEDING PAGE BLANK NOT FILMED



Figure 1 (continued)

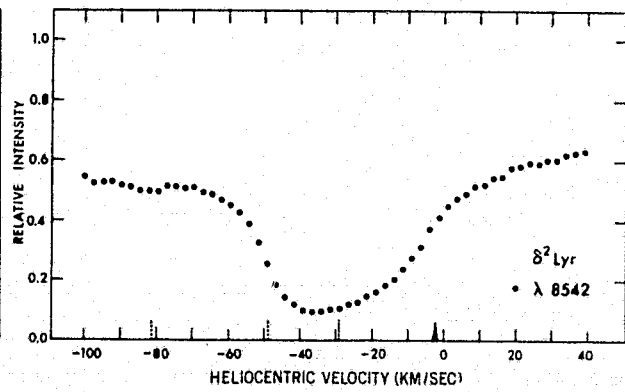
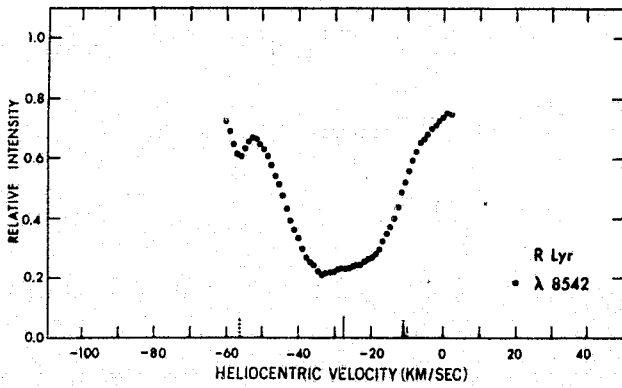
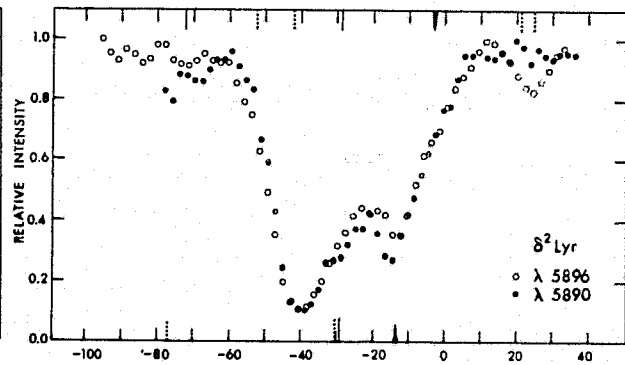
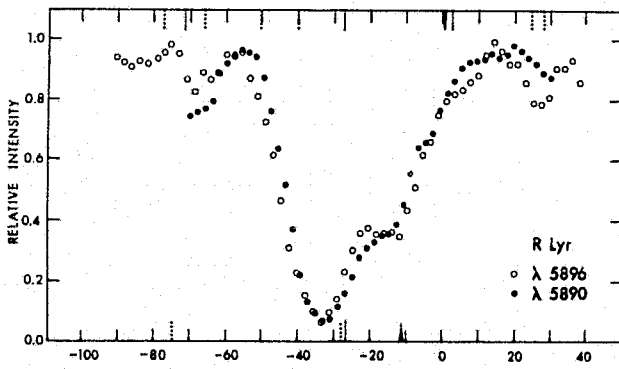
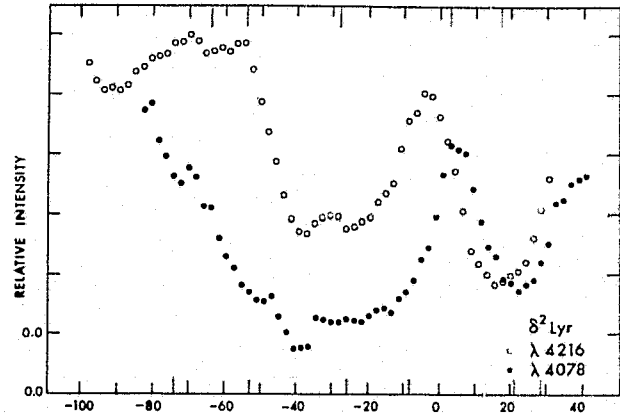
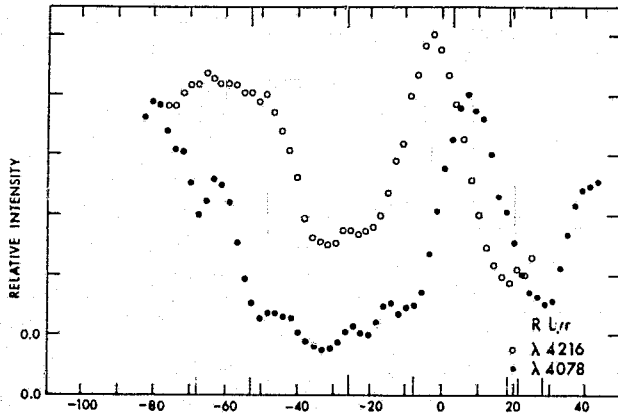


Figure 1 (continued)

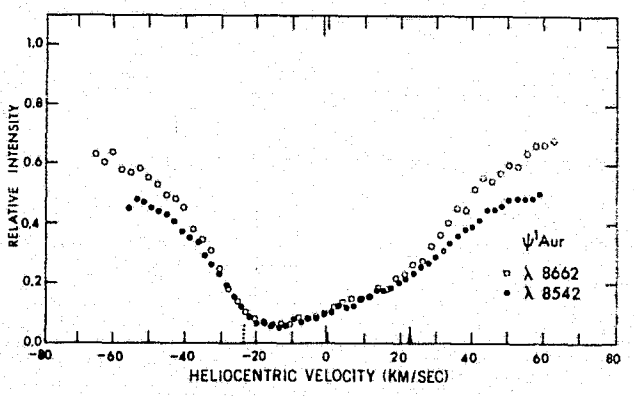
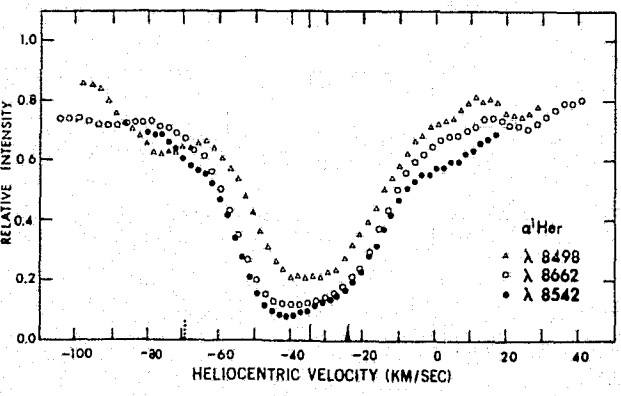
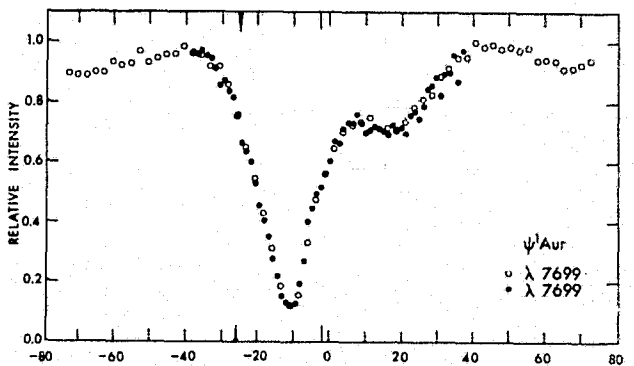
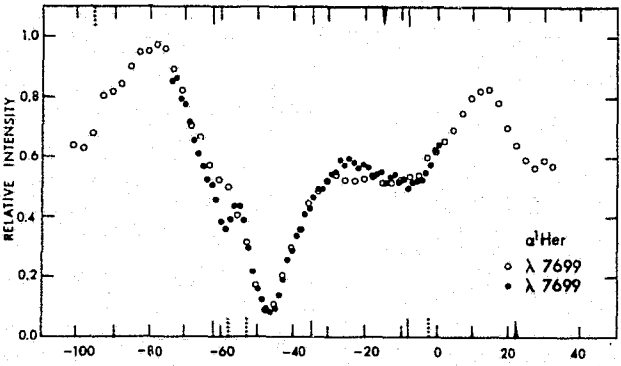
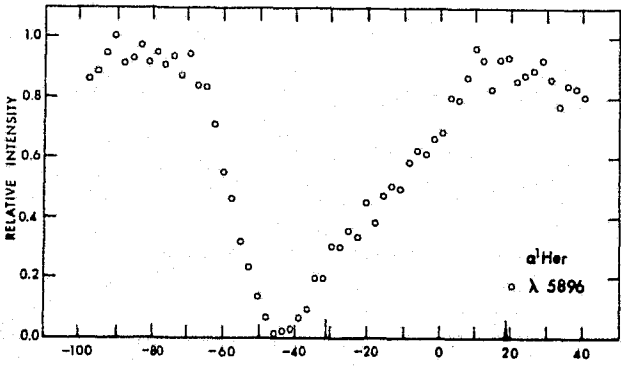
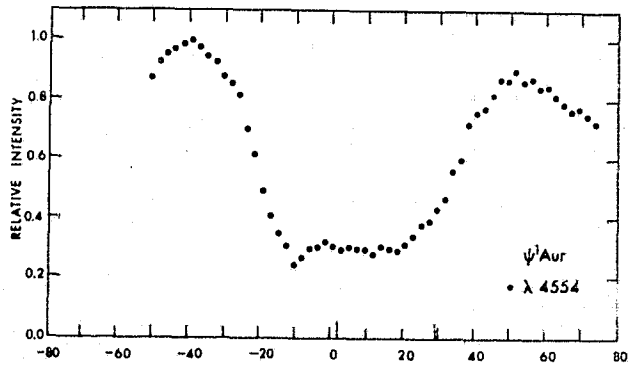
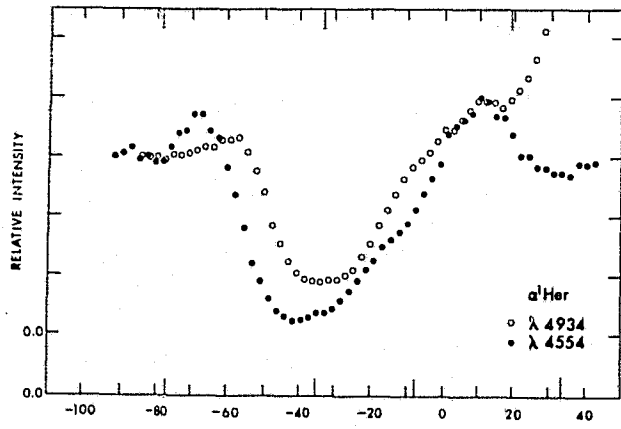


Figure 1 (continued)

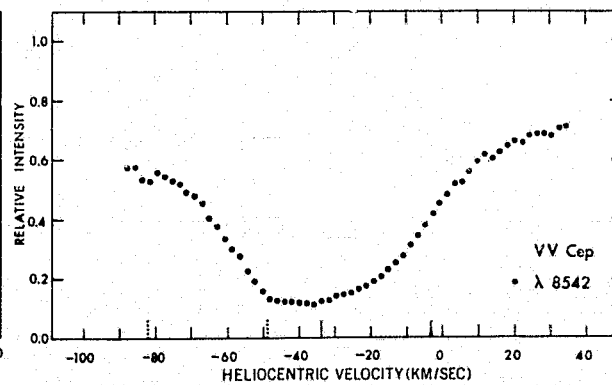
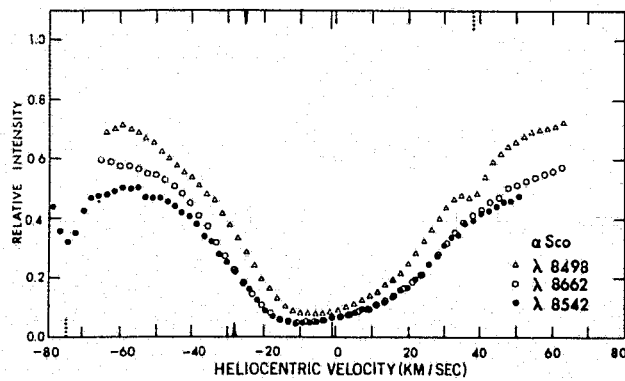
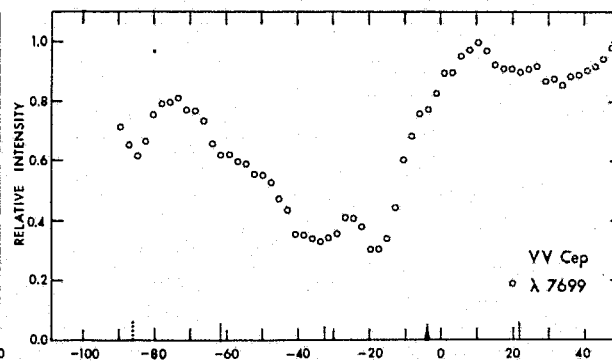
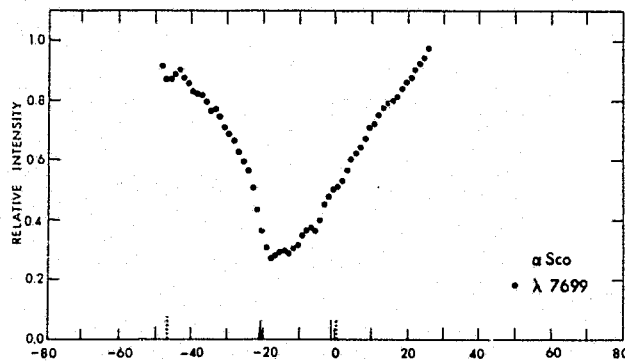
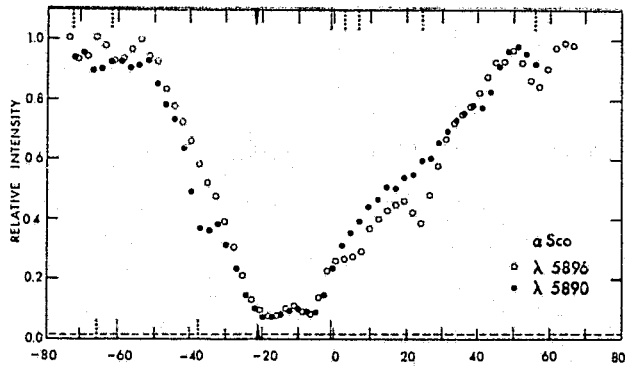
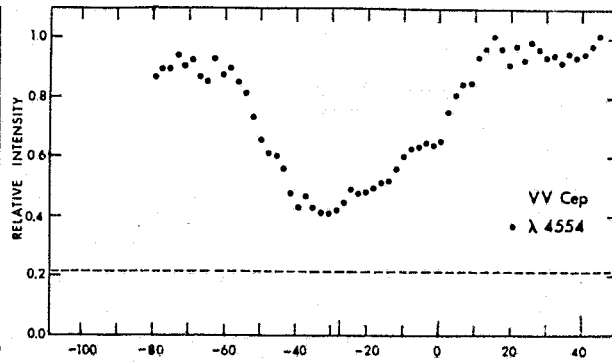
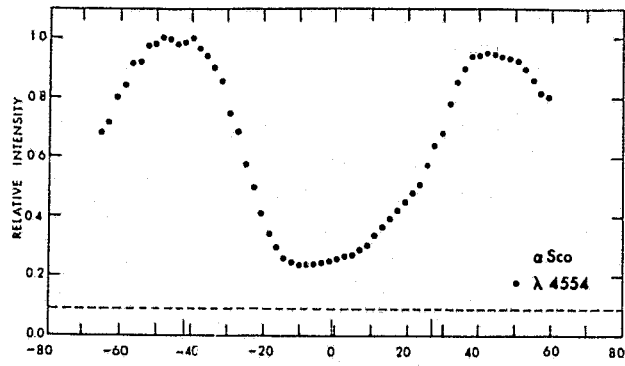


Figure 1 (continued)

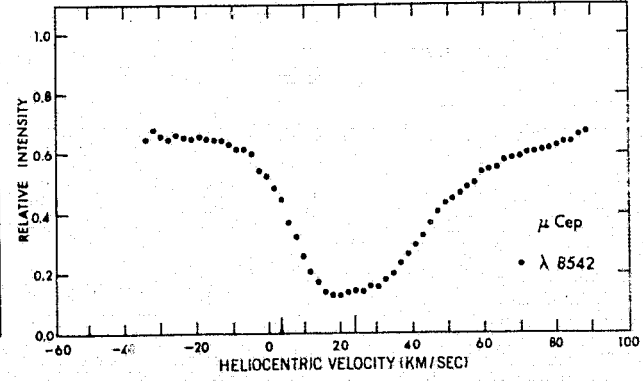
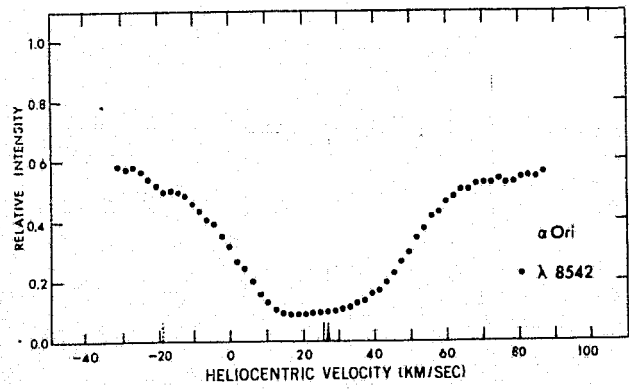
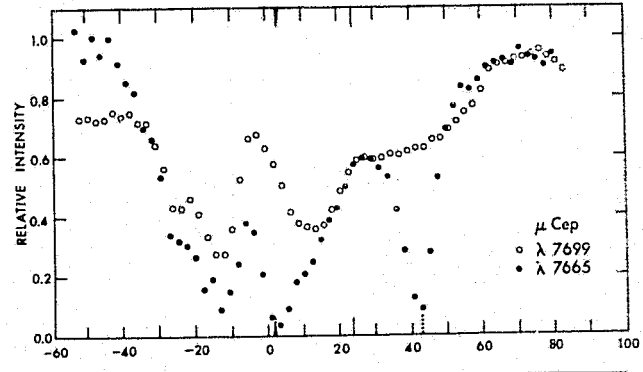
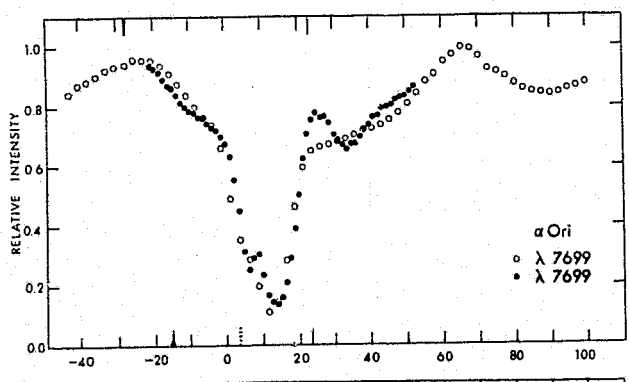
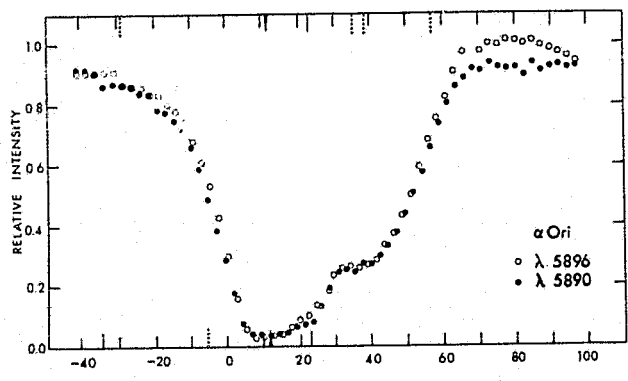
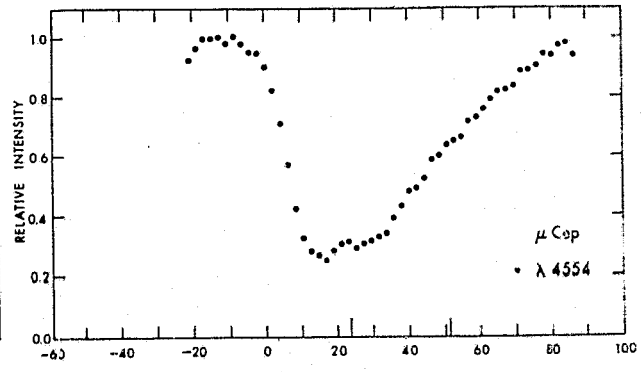
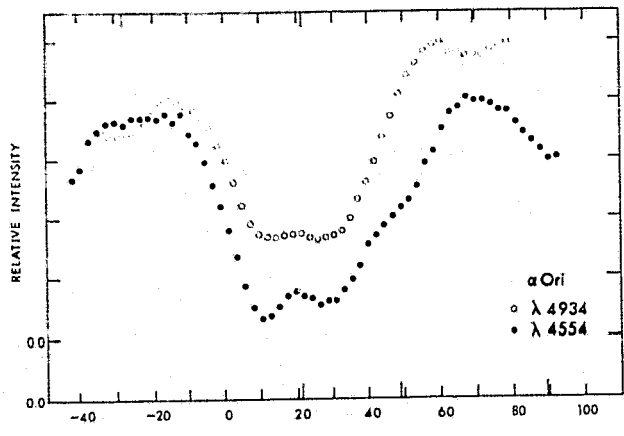


Figure 1 (continued)

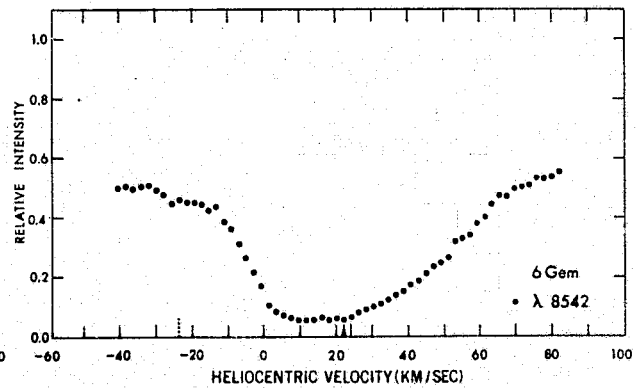
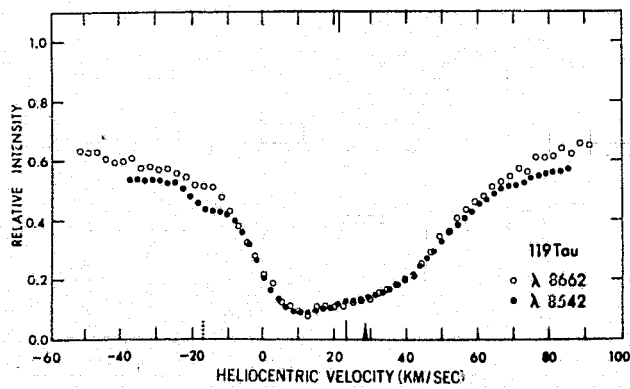
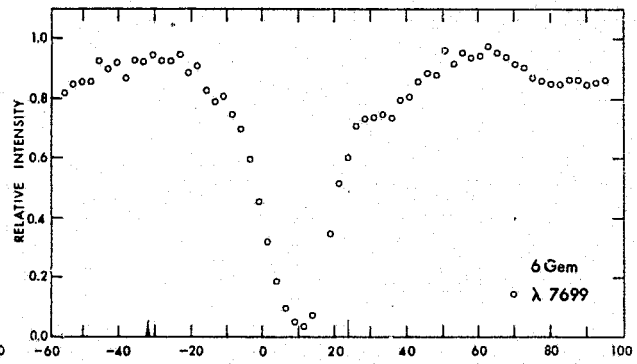
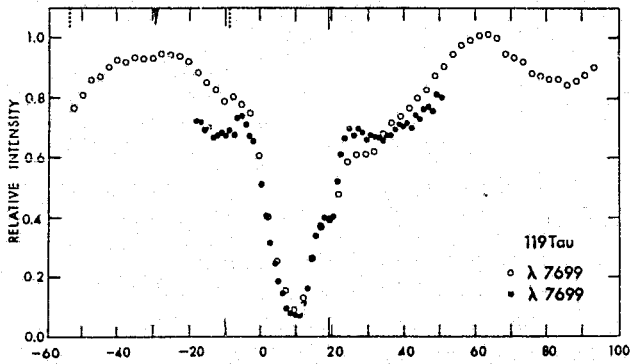
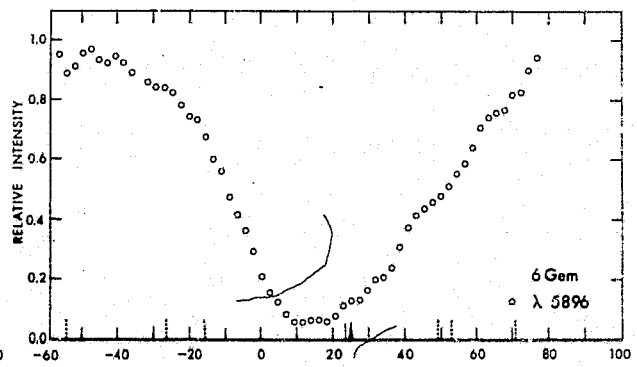
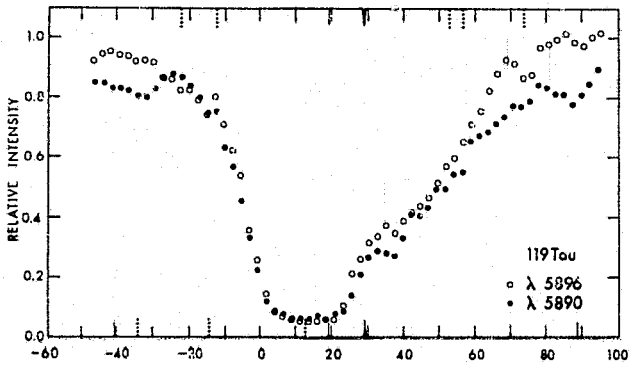
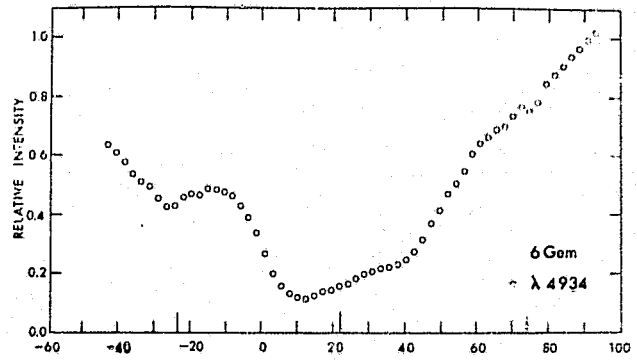
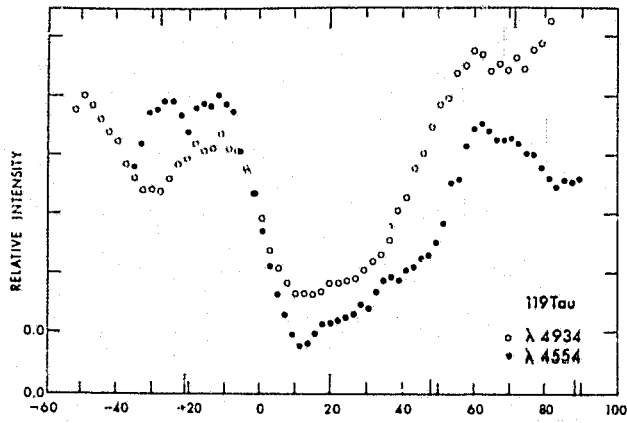
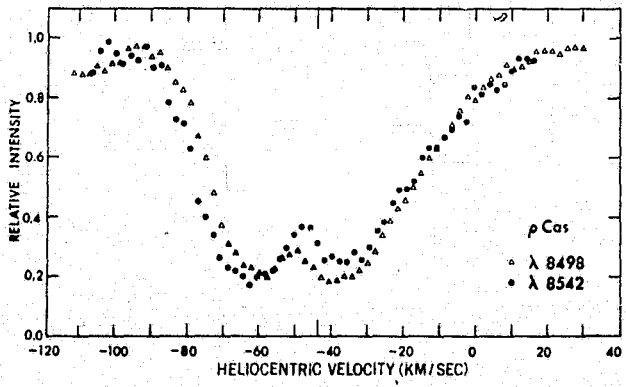
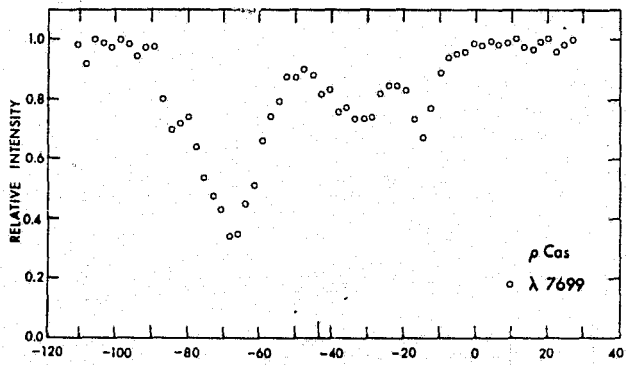
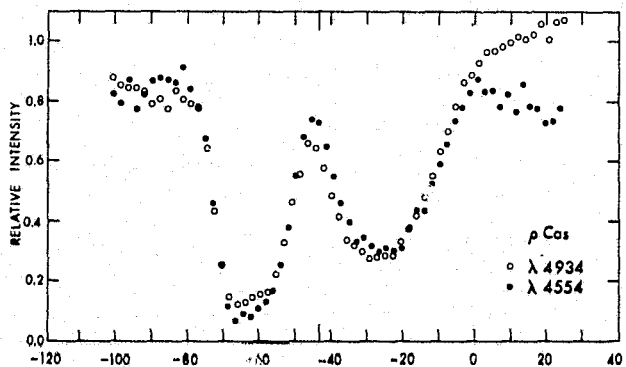
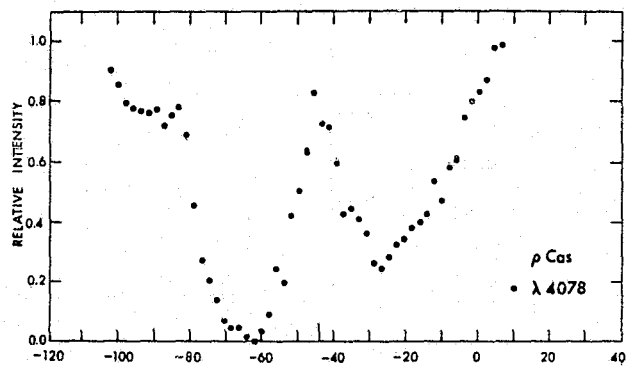


Figure 1 (continued)



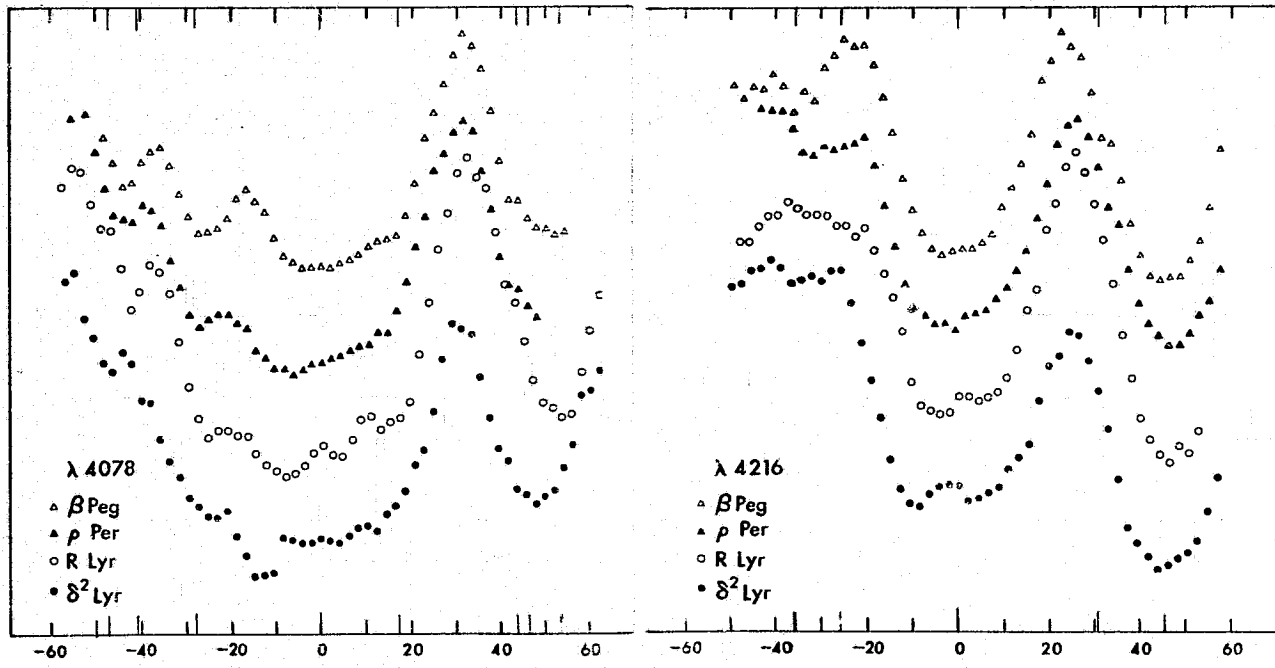


Figure 3

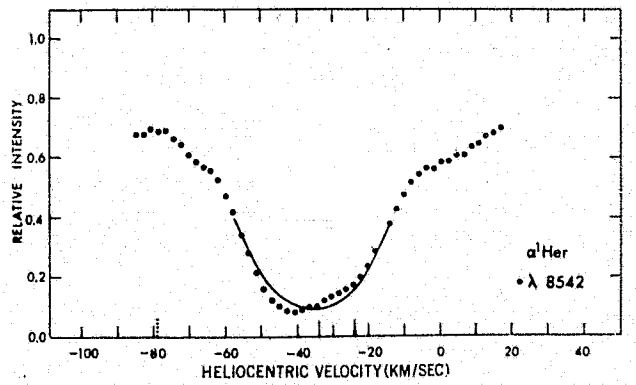
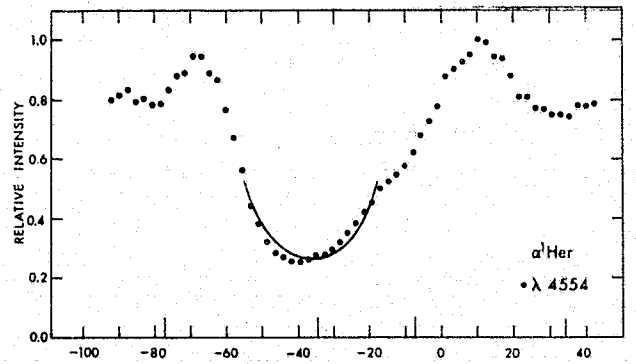
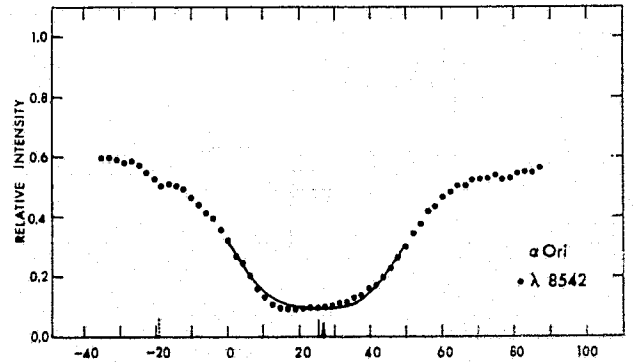
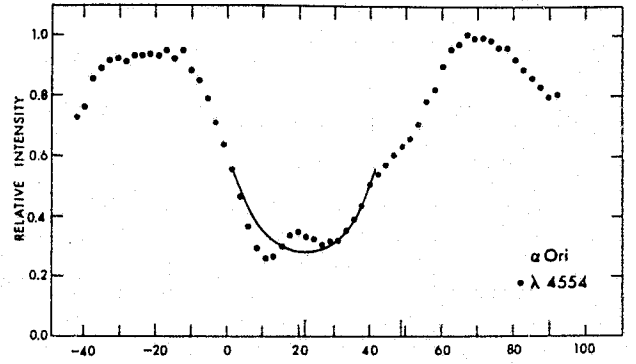




Figure 4

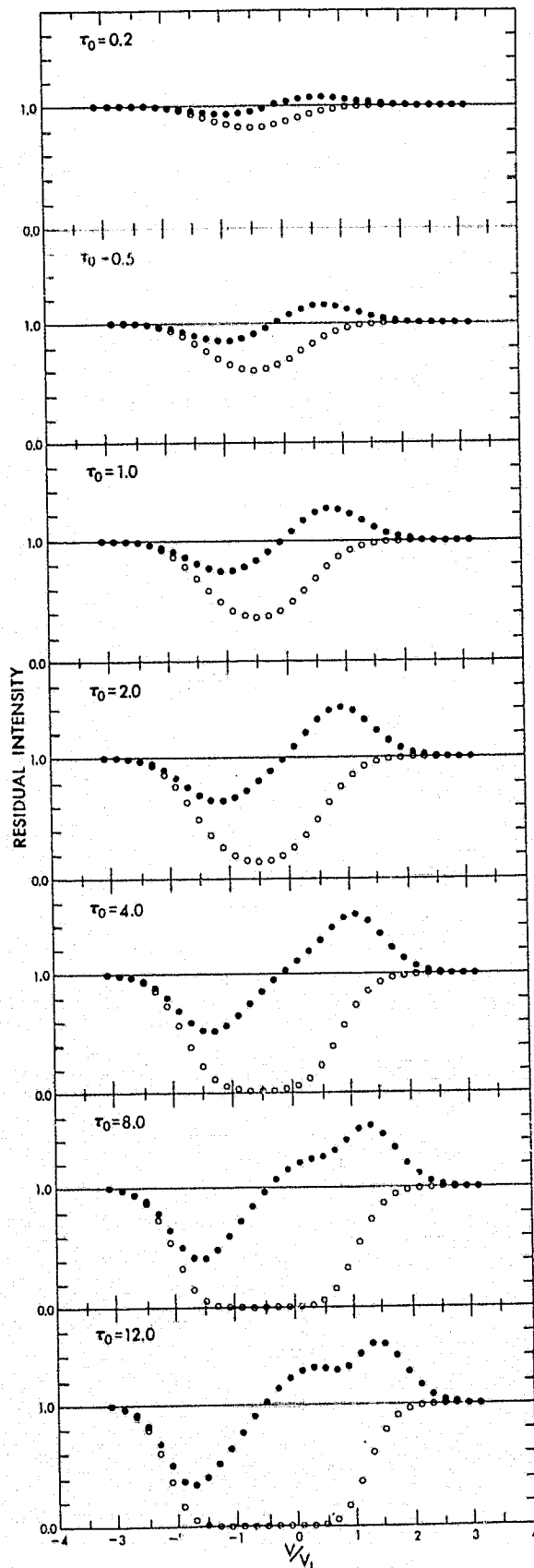


Figure 5

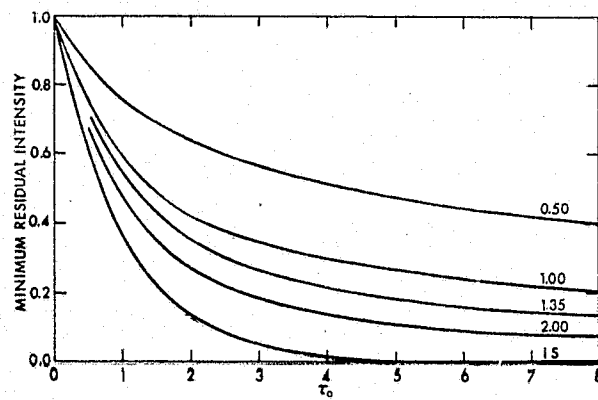


Figure 6

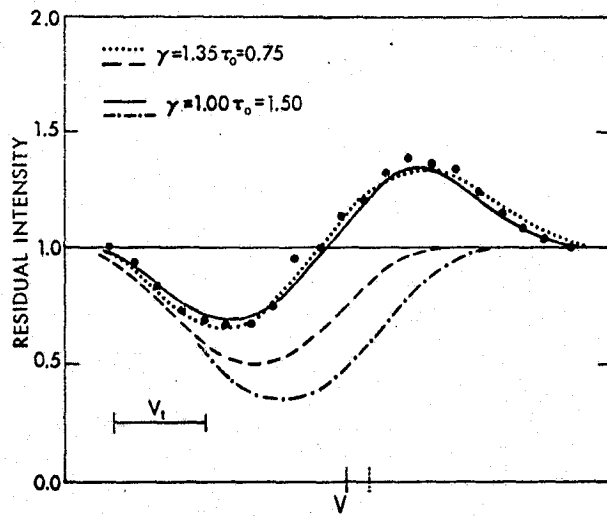


Figure 7

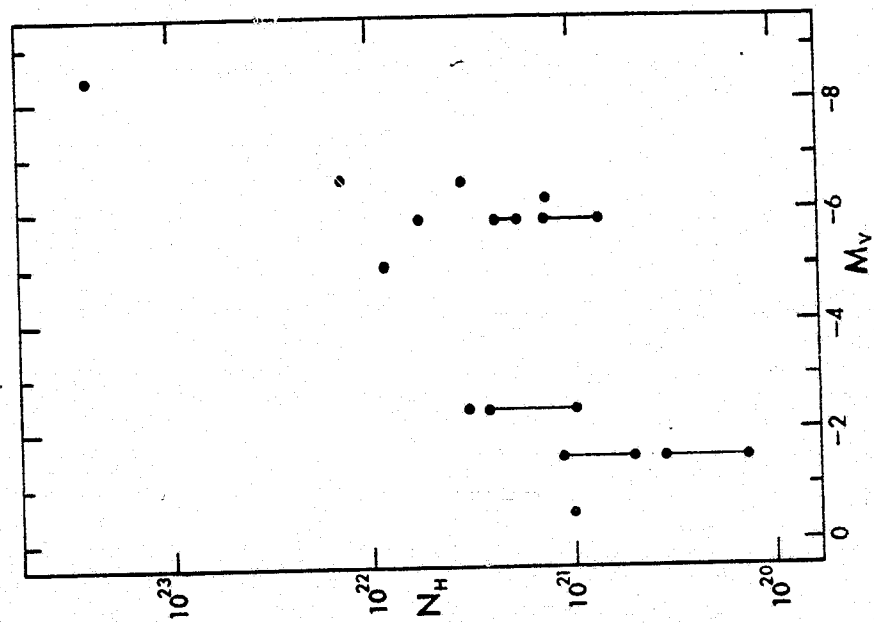


Figure 8

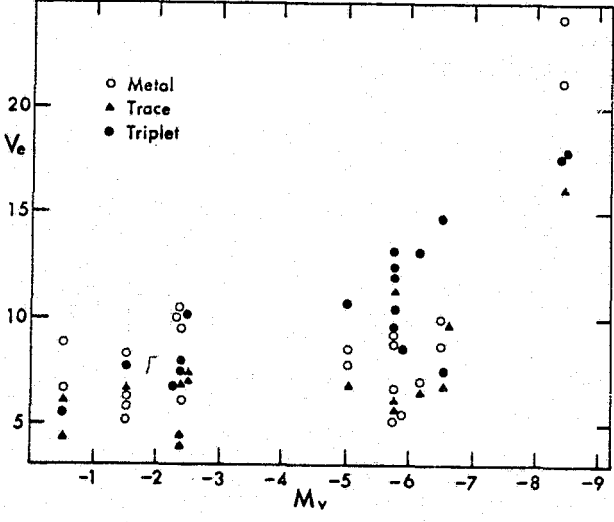


Figure 9

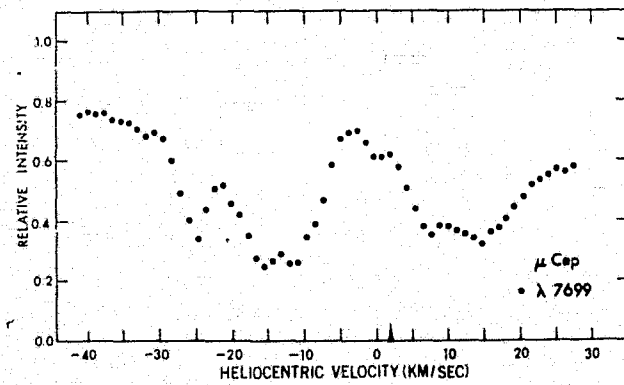
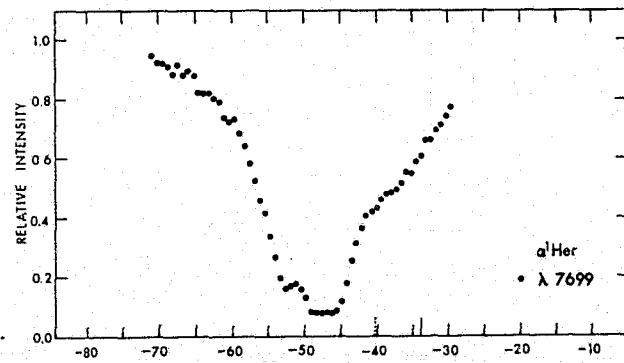
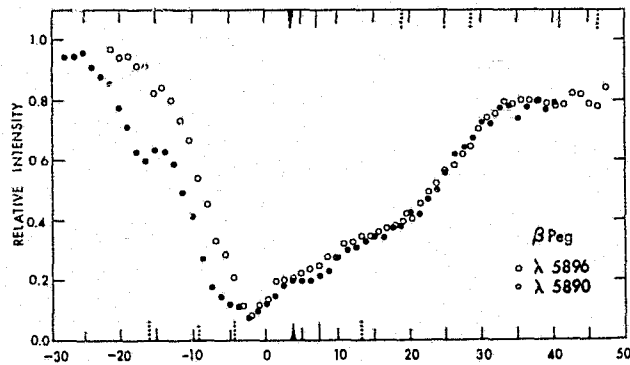
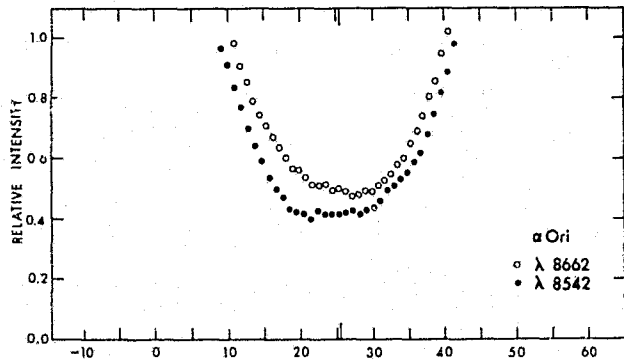


Figure 10

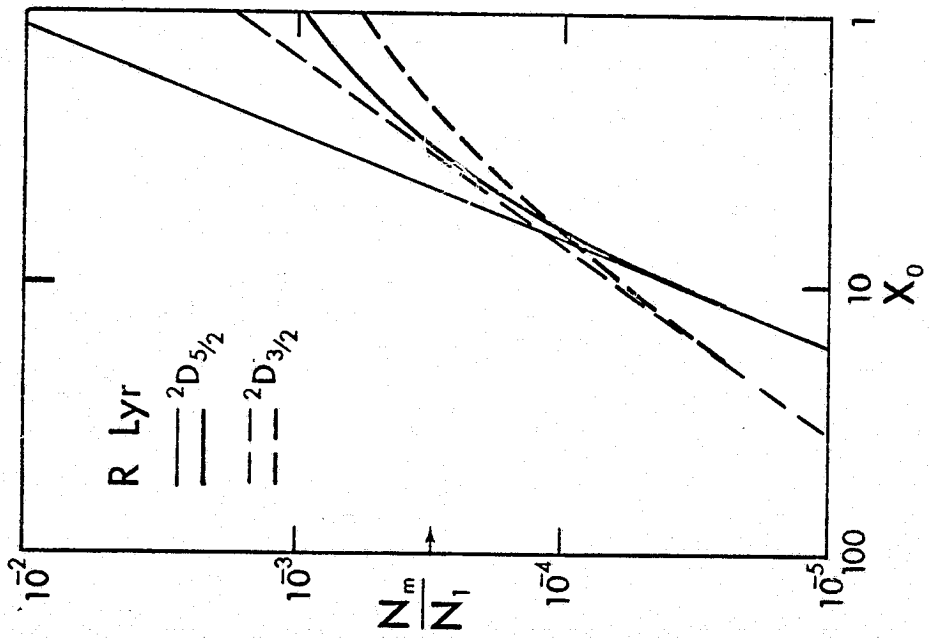


Figure 11

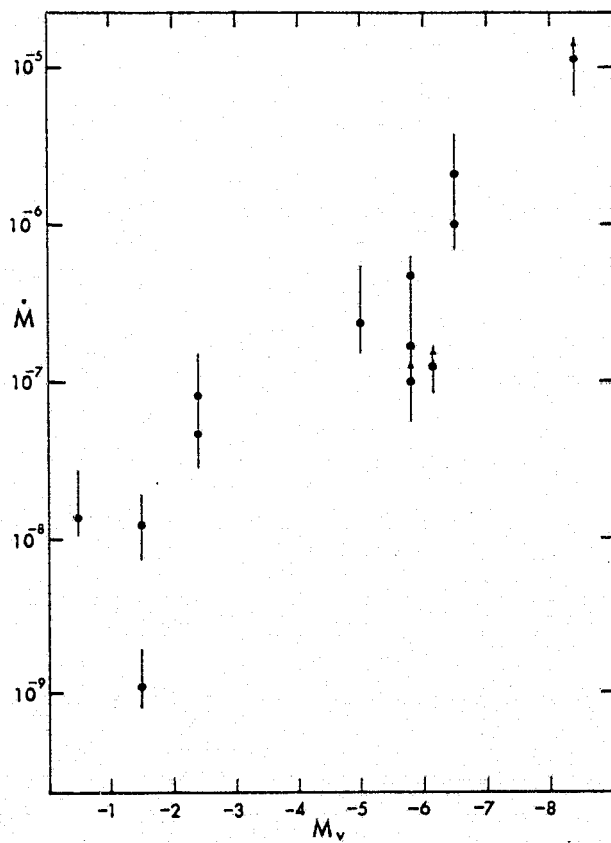




Figure 12

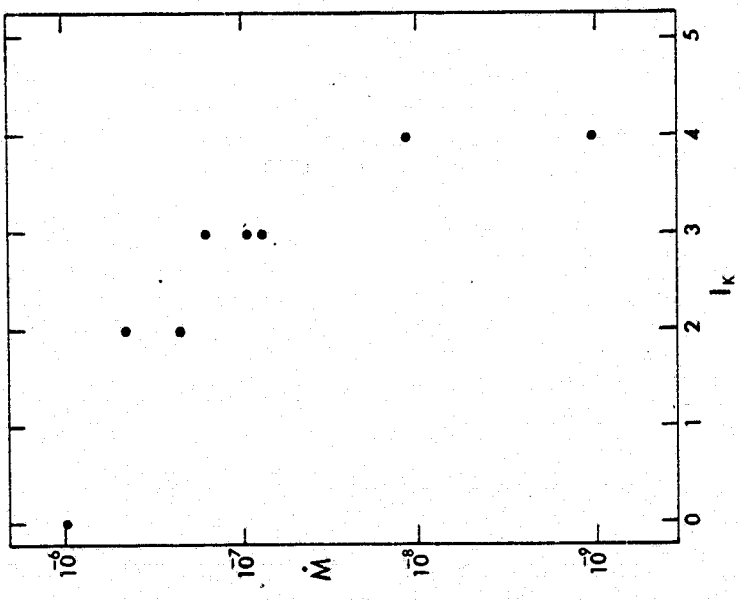
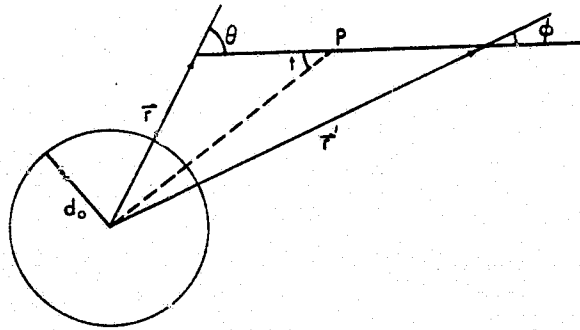
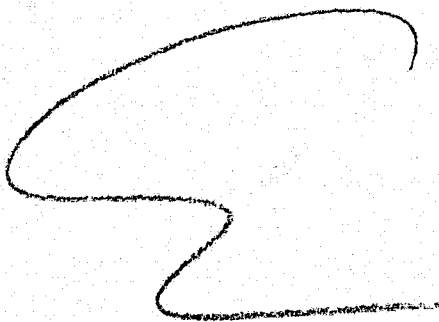


Figure A1



 HVD